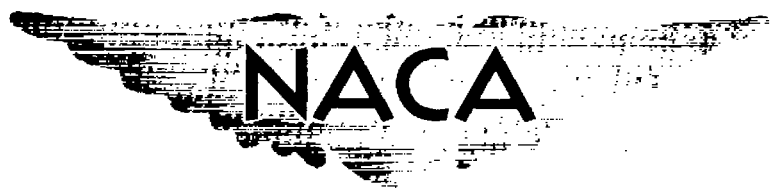


CONFIDENTIAL

CZ

UNCLASSIFIED



RESEARCH MEMORANDUM

EXPERIMENTAL SHOCK CONFIGURATIONS AND SHOCK LOSSES IN A
TRANSONIC -COMPRESSOR ROTOR AT DESIGN SPEED

By Genevieve R. Miller and Melvin J. Hartmann

Lewis Flight Propulsion Laboratory
Cleveland, Ohio

CLASSIFICATION CHANGED

To UNCLASSIFIED

RECEIVED COPY

JUN 5 1958

By authority of LPA #12 ^{refut} Date 3/18/68
js H

LANGLEY RESEARCH LABORATORY
LIBRARY, NACA
LANGLEY FIELD, VIRGINIA

CLASSIFIED DOCUMENT

This material contains information affecting the National Defense of the United States within the meaning of the espionage laws, Title 18, U.S.C., Secs. 793 and 794, the transmission or revelation of which in any manner to an unauthorized person is prohibited by law.

NATIONAL ADVISORY COMMITTEE FOR AERONAUTICS

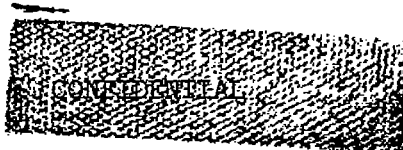
WASHINGTON

June 5, 1958

CONFIDENTIAL

UNCLASSIFIED

NACA RM E58A14b



NATIONAL ADVISORY COMMITTEE FOR AERONAUTICS

RESEARCH MEMORANDUM

EXPERIMENTAL SHOCK CONFIGURATIONS AND SHOCK LOSSES IN A

TRANSONIC-COMPRESSOR ROTOR AT DESIGN SPEED

By Genevieve R. Miller and Melvin J. Hartmann

SUMMARY

Barium titanate crystals were used to obtain the instantaneous static-pressure variation from one blade to the next in a transonic-compressor rotor. By observing the static-pressure variation at several axial positions along the blade tip, the shock configuration was established. Such data were taken over a range of operating conditions from rotor choke to rotor stall at the rotor design speed (1300 ft/sec), for which the tip relative Mach number was about 1.34. The experimental data were used to find the passage shock losses and were compared with analytical and approximate methods of estimating shock loss and location.

The crystal static-pressure pickups indicated a passage shock, the location and shape of which varied considerably with operating conditions. At the lowest back pressure a shock wave originated a short distance ahead of the leading edge of the blade and extended across the passage, falling behind the preceding blade. As the back pressure increased, the shock moved up into the passage between the blades (without moving appreciably forward of the leading edge) to become almost normal to the mean flow at the point of rotor peak efficiency. Near the point of rotor stall (highest back pressure), the shock was located a considerable distance ahead of the blade leading edge.

A computed shock-loss coefficient of 0.19 was obtained at the point of rotor peak efficiency. The shock loss decreased at incidence angles above and below this operating condition. At rotor peak efficiency the shock losses were the major losses. However, at high incidence angles, the blade-profile losses appeared to be the principal source of losses. The distance of the bow wave ahead of the blade leading edge agreed reasonably well with the analytically predicted distance and varied considerably with rotor operating conditions. The bow wave contributed a very small part of the total loss. Near the rotor peak-efficiency point, the experimental results agreed reasonably well with those predicted by a simplified analysis.



INTRODUCTION

Reference 1 proposed a simplified flow model for supersonic blade elements in transonic-compressor rotors. The reference investigation considered the flow model that may be obtained at minimum over-all blade-element loss. The shock shape (path of the shock across the passage from suction surface to pressure surface) and location were assumed, and an approximate shock-loss coefficient was obtained for the minimum-loss condition. The passage shock-loss coefficient was obtained from an average of the upstream Mach number and the suction-surface Mach number at the point of intersection of the shock with the suction surface. For the 17 transonic-compressor rotors considered in the analysis, the method of approximating shock loss revealed that 0.35 to 0.55 of the total loss was in the form of passage shock loss.

In reference 2 the effects of shock losses were measured at the blade-row exit by a hot-wire anemometer for the blade-element minimum-loss operation at various speeds. The shock-loss coefficients measured from blade to blade were compared with the analytical shock-loss coefficients. This comparison of blade-to-blade loss coefficients indicated that the assumed flow conditions were substantiated by the measured data. The shock location apparently varied with relative inlet Mach number and had a considerable effect on the magnitude of the computed passage shock loss.

Reference 1 includes a qualitative description of the variation in the passage shock configuration (shape and location) from low back pressure (choke) to high back pressure (stall). At low back pressures the shock configuration is swept well back into the blade passage; that is, the passage shock extends from a point near the nose of the blade to a region near or even downstream of the trailing edge of the next blade and may include many branches from both the pressure and the suction surface of the passage. As the back pressure increases, these branches probably come together and form a shock line that can be approximated by a straight line normal to the mean passage. Then, as the back pressure further increases, the shock shape remains nearly the same but the shock moves upstream. In references 1 and 2, the only shock configuration used to calculate the shock losses was that for moderate back pressure, which was presumed to be near a design, or blade-element minimum-loss, point. Before the variation of passage shock loss with operating conditions can be determined, it is necessary to know the shock shapes and locations in the blade passage as they vary with compressor operating conditions.

In order to investigate these shock effects, a transonic-compressor rotor was operated at design speed (1300 ft/sec, ref. 3) with instrumentation that made possible the observation of shock shape and location. Barium titanate crystal probes were installed at four axial stations to indicate the instantaneous static-pressure variations over the blade tip

for a range of operating conditions. Thus, the shock configuration at the rotor tip was established, and the variation in passage shock loss over this range of operating conditions was determined. The shock-wave location ahead of the blade leading edge was also estimated from these crystal data and was compared with the analytical method of locating the bow wave ahead of the blades, as developed in reference 4. The magnitude of the losses associated with the extended bow wave was determined analytically by the methods of references 5 and 6.

APPARATUS AND PROCEDURE

Compressor Rotor

The compressor rotor used in this investigation is shown in figure 1, and the test installation in figure 2. The compressor design and performance are given in detail in reference 3. The principal design features are as follows:

- (1) Inlet tip diameter, 16 inches
- (2) Inlet tip speed, 1300 feet per second; absolute inlet axial Mach number at the mean radius, 0.625; no inlet guide vanes
- (3) Blade chord length, 1.75 inches; tip solidity, approximately 1.0
- (4) Total-pressure ratio, approximately 1.60
- (5) Discharge tip diameter, 15.5 inches; tip diffusion factor, approximately 0.41
- (6) Double-circular-arc blade sections
- (7) Blade thickness at the tip, 5 percent of the chord

Instrumentation

The instrumentation used in this investigation is described in reference 3 for the instrument stations indicated in figure 2. In addition, four barium titanate static-pressure pickups were located at axial stations on the outer wall to measure the instantaneous static-pressure rise caused by the shock at the blade tip.

Figure 3(a) is a photograph of the barium titanate static-pressure pickup, and figure 3(b) shows the mechanical details. The barium titanate crystal is a circular cylinder approximately 1/16 inch in diameter and

4696

CT-1 back

approximately 1/16 inch long. The cylindrical crystal is glued to an insulating member through which a wire is passed near the base of the crystal. Electrical contact from the crystal to the wire is made by a coating of silver conducting paint. The end of the crystal is closed by an adhesive cap and is surrounded by a metal probe mount, leaving a space of approximately 0.010 inch between the crystal and the metal. The barium titanate static-pressure pickup is mounted in the wall of the compressor housing so that the crystal is flush with the wall.

The variation in static pressure against the crystal results in a deformation and generates a small electromotive force. This voltage is large enough to be amplified and observed on an oscilloscope screen. The circuit diagram is shown in figure 4. The signals were first amplified and sent into the oscilloscope, and the oscilloscope sweep frequency was synchronized with the passing blades by a magnetic pickup. The signal from the barium titanate crystal was photographed on the oscilloscope screen. The frequency of the crystal and the associated electronic circuit is estimated to be at least 80,000 cps, which is well above the blade frequency (approx. 8400 blades/sec).

Crystal pickups were installed at four axial stations in the compressor-rotor housing, as shown in figure 5(a). As the rotor blades passed the crystal pickups, the instantaneous static-pressure variation was indicated along the lines shown in figure 5(b). Each crystal probe indicated a drop in static pressure as the blade suction surface passed. Between the rotor blades, the rapid increase in static pressure was taken as the location of a shock front. By establishing the distance of the shock front from the blade pressure surface at each of the crystal probe positions, a passage shock line was established.

Data for comparison with analytical results and with the experimental data of reference 3 were obtained at five operating conditions from open throttle to stall at the design speed of 1300 feet per second. The experimentally determined shock shape and location were then used to determine a passage shock loss. The methods used to determine a passage shock loss are similar to those of reference 2. The symbols used in the analysis are given in appendix A and the computation methods in appendix B. The analytical location of and loss due to the extended bow wave were determined by the methods of references 4 to 6.

RESULTS AND DISCUSSION

The aerodynamic performance of the compressor rotor necessary for analysis of the losses is briefly described and compared with other experimental and analytical results.

Compressor Performance

The performance curves at design speed (1300 ft/sec) are taken from reference 3 and are shown in figure 6. The pressure-ratio variation from open throttle to stall was normal for a transonic compressor, and the peak adiabatic efficiency at design speed was 0.815. The operating conditions at which crystal data were taken, designated by the letters A, B, C, D, and E on the curves, are used for reference in the following discussion.

The blade-element performance is indicated in figure 7, where relative total-pressure-loss coefficient, relative inlet Mach number, diffusion factor, and work coefficient are plotted against incidence angle for a blade element at 11 percent of annulus height from the outer wall. The blade-element performance curves were taken from reference 3, and the crystal data points A, B, C, D, and E have been superimposed. The variation of loss coefficient with incidence angle at 1300 feet per second results in a very steep curve having a section that is nearly vertical at the low-incidence end.

The crystal data were obtained at the blade tip and therefore cannot be directly compared with those obtained at 11 percent of annulus height. Consequently, a "pseudo" tip-element performance was obtained by extrapolating radial variations of total-pressure-loss coefficient, relative Mach number, and incidence angle to the outer wall. These tip-element performance parameters are shown in figure 8 and are used for comparison with the values computed from the crystal data. The loss coefficient for the blade element at 11 percent of annulus height is plotted in figure 8 against incidence angles corresponding to the pseudo-tip data. Since the loss-coefficient gradient becomes steep in the tip region, an extrapolation of this type must be considered approximate.

Interpretation of Static-Pressure Variations from Crystal Probes

Determination of shock configuration. - Figure 9 is a photograph of the oscilloscope screen showing a typical trace of static-pressure variation obtained by the crystal pickup. The drop in static pressure from the blade pressure surface to the suction surface is clearly shown. The static pressure remains low until it encounters the shock, where a very rapid rise in static pressure occurs.

The static-pressure variations obtained at the four crystal-probe stations were used to determine the shock location relative to the rotor blades. A series of such static-pressure variations is shown in figure 10 for the compressor over-all maximum-efficiency operating condition (point C in fig. 8). At crystal-probe station 1, which is close to the leading edge, the static-pressure rise occurs quite close to the blade pressure

surface. At station 2 the static-pressure rise from the shock occurs approximately halfway across the blade passage, and at station 3 the static-pressure rise is obtained somewhat closer to the blade suction surface. At station 4 the static pressure begins rising almost as soon as the blade suction surface has passed. The shock must therefore be very close to the intersection of the passage shock and the blade suction surface. A sketch of the blade passage indicating the shock location obtained from these oscilloscope traces is also given in the figure.

Variation of shock configuration with rotor operating conditions. - The shock configurations obtained for five operating conditions at design speed are illustrated in figure 11. The rotor performance curve from figure 6 is also included to orient the data. For operating condition A (low back pressure), the shock moves back into the blade passage and, according to the crystal data, apparently misses the blade suction surface. This suggests that, at the open-throttle condition, high supersonic velocities exist along the blade suction surface and may exist near the exit of the compressor rotor. However, there is undoubtedly some compression shock system at the blade trailing edge, which might have occurred downstream of the last crystal probe and therefore out of the region of observation. As the back pressure is increased to operating condition B (fig. 11(b)), the shock moves forward on the blade suction surface and becomes more nearly normal to the blade passage. This operating condition is still on the choke line. At operating condition C (fig. 11(c)), the back pressure has been increased further to near the point of compressor maximum efficiency. At this condition, the shock remains about normal but moves forward somewhat in the passage. As the back pressure is increased further (operating condition D), the shock moves forward in the blade passage and away from the leading edge of the blade. At the highest back pressure (near rotor stall, fig. 11(e)), two shock lines show the extent of the variation in shock location. Possible explanations for this variation are: (1) The shock is unstable and is indicated by the crystals at various positions in the region of instability; and (2) the shock location differs from passage to passage because of slight geometric variations in the blades. Even though the shock location is not uniquely defined at the highest back pressure (condition E), it is apparent that the region of the shock is moved well forward in the blade passage and the bow wave stands a considerable distance ahead of the blade leading edge. It is significant that, in this compressor rotor, the change in shock configuration over the range of operating conditions is essentially that proposed in the model of reference 1.

Under certain operating conditions, forked or multiple shock patterns may have existed nearly parallel to the path of the crystal static-pressure pickup, in which case the pattern could not have been observed with the instrumentation used in this investigation.

4696

Average static-pressure distribution across blade row. - The shock configurations observed would affect the static-pressure variation measured along the compressor-rotor outer wall. Static-pressure taps over the tips of the rotor blades measure some average along a line parallel to the crystal-probe line as indicated in figure 11. The average static-pressure variations over the rotor blade tips are shown in figure 12 for the operating conditions A, B, C, D, and E. For operating condition A, the average static pressure decreased over the first half of the blades and then increased back in the rotor. This apparently is a result of the high-velocity region extending back along the blade suction surface and the averaging effect of the static-pressure taps. As the back pressure on the rotor increased, the initial drop in average static pressure was less and the region of minimum average static pressure moved toward the leading edge of the rotor blade. The shock configurations shown in figure 11 are responsible for the average static-pressure variations indicated in figure 12.

Variation of Shock Losses

Blade-to-blade variation of shock losses. - After the shock shape and location have been determined from the crystal probes, the passage shock loss can be computed. The methods of computation (appendix B) are similar to those of reference 2, which assumed a shock configuration that moved forward in the passage with increasing incidence angle and had the same slope as a line drawn perpendicular to the midchannel (mean-camber) streamline through the nose of the next blade. For a known upstream flow direction and Mach number, the expansion system about the blade suction surface can be computed for the region ahead of the passage shock. Thus, the Mach number and flow direction can be determined at any point along the face of the shock, and the angle that the shock makes with the stream can be used to compute the local shock loss.

The results of this computation are shown in figure 13, where the total-pressure shock-loss coefficient is plotted against percentage of passage distance from the blade suction surface to the pressure surface. The shock configurations from figure 11 are reproduced to show the relative positions of the shock for the five operating conditions. At condition A, where the shock was swept back into the blade passage and was quite oblique to the stream, the loss coefficient was low across the blade passage and reached an estimated maximum value of 0.10 (based on assumed shock conditions at the blade exit). At a higher back pressure (condition B), where the shock became more nearly normal to the blade passage, the shock loss increased sharply, especially in the region of the suction surface. This is mainly a result of the change in the angle of the shock. At operating condition C near the rotor maximum-efficiency point, the shock has moved forward somewhat more. However, there seems to be little difference in loss coefficient as the shock moved forward from the B to

██████████

the C operating condition. As the back pressures were increased further to operating condition D, the shock shape was not changed particularly, but the change in incidence angle and the movement of the shock to a lower Mach number region resulted in a reduction in the passage shock loss, as shown in figure 13(d). This effect is observed further in figure 13(e), where the two limiting shock-pattern locations were considered. In this region, which is well forward on the blade, the shock occurred at a relatively low Mach number with the resultant reduction in shock loss.

Variation of mass-averaged passage shock losses. - The mass-averaged passage shock-loss coefficient at each operating condition is shown in figure 14. (Operating condition A is not shown because the mass-averaged value of the passage shock loss cannot be estimated unless the shock intercepts the suction surface.) It is observed that the computed passage shock loss is the highest in the region of moderate back pressures (points B and C) and decreases at the higher back pressures (points D and E). The loss coefficient is approximately 0.19 at points B and C and decreases to approximately 0.11 at the highest back pressure (point E).

Also shown in figure 14 is the pseudo-tip-element loss. A direct comparison cannot be made between the measured tip-element loss data and the computed shock-loss values because the pseudo-tip losses are probably overestimated. The important point to be noted here is the difference in trend between the measured over-all losses and the calculated passage shock losses. This difference can be attributed to factors other than shock losses, as discussed in a later section.

Experimental shock shape and location compared with approximate methods. - In figure 15 the experimental shock location near the point of maximum rotor efficiency (condition C) is compared with that obtained by the methods of reference 1. In that reference, the shock was assumed to have intercepted the suction surface at a point where a line drawn normal to the midpassage streamline and passing through the nose of a blade would strike the suction surface. The point designated in reference 1 is shown in figure 15 as the intersection of the dashed line and the suction surface. Reference 1 then assumed that the passage shock extended across the entrance region, falling some distance (which was not specified) ahead of the nose of the blade. Operating condition B is on the choke line, and the intersection of the shock with the suction surface apparently falls behind the point used in the preliminary analysis. Condition C, which is the maximum-efficiency point of the rotor, indicates that the shock is very close to the configuration used in the preliminary study.

Also shown in the figure are the mass-averaged passage shock-loss coefficients for operating conditions B to E and the shock-loss coefficients obtained by the methods of reference 1 for conditions B and C. This simple approximation gives a loss coefficient of about 0.190 to 0.192 as compared with loss coefficients for the corresponding points of this

investigation of about 0.191 to 0.194. The agreement of total-pressure-loss coefficients obtained by the two methods is striking.

The foregoing comparison indicates that the methods of reference 1 estimated a location of the shock which was reasonably close to that observed with the static-pressure crystal pickups, and the assumed magnitude of the Mach number along the shock near the suction surface may be justified. However, the generally accepted concepts of boundary-layer development along the rotor blade would indicate that the calculated suction-surface Mach number may not actually be realized. On the other hand, reference 1 assumes that the Mach number at the leading edge of the blade is equal to the upstream Mach number while the expansion field about the blade develops a higher Mach number along the face of the shock in the vicinity of the leading edge. These two opposing considerations, along with the assumption that the shock is normal to the flow, apparently cancel one another in the data of the present investigation.

The movement of the passage shock with operating conditions was essentially as suggested in reference 1, and the magnitude of the shock loss at the rotor peak-efficiency point was remarkably close to that approximated by the methods of reference 1. It is not certain whether the apparent agreement between the two methods is peculiar to this rotor or whether it would generally be obtained in transonic-compressor rotors.

Bow-Wave Losses

It has usually been assumed that the passage shock and the bow wave constitute the shock losses and that these form a continuous shock line extending from the blade suction surface past the nose of the following blade and on to infinity. The bow wave and the passage shock are divided by the stagnation streamline. The following discussion considers the analytical method available for estimating the location of the bow wave and the magnitude of the losses associated with the bow wave. The calculated shock losses are compared with the values experimentally measured in this investigation.

Analytical method of predicting location of bow wave. - The analytical methods developed in references 4 and 5 are suitable for approximately locating the bow wave and calculating the losses associated with it. Figure 16 is a sketch of the flow model used. The first step in such an analytical approach requires that a stagnation streamline be determined. This can be determined in the entrance region of a supersonic cascade where it is assumed that for the region ahead of the shock the expansion region completely describes the flow, since along each expansion wave the flow direction and the Mach number are known and the mass flow between stagnation streamlines can be established. The required length along each expansion wave from the suction surface to the stagnation streamline

can be determined from continuity, and thus the stagnation streamline can be traced to the point of the shock intersection with the stagnation streamline. The calculation details are given in appendix B. The upstream spacing between stagnation streamlines and the applicable extent of the calculation are indicated in figure 16.

Also shown in figure 16 is the distance h , which is defined as the stagnation-streamline deflection or the height of the blade above the stagnation streamline. For the present investigation this distance was found by extending the stagnation streamline past the nose of the blade and computing the distance normal to the stagnation streamline from the nose of the blade. With this value of h and an effective Mach number ahead of the bow wave, the methods outlined in references 4 to 6 can be used to calculate the distance of the bow wave ahead of the blade (L in fig. 16). These methods are summarized in appendix B.

Variation of streamline deflection and bow-wave location. - The variation in the dimensionless height h/Y_{SB} is shown in figure 17(a). At the lowest back-pressure point, h/Y_{SB} is about 0.02. The value of h/Y_{SB} increases with back pressure (that is, with incidence angle) until a value of approximately 0.08 is obtained at the highest back-pressure point.

The calculated variation in the dimensionless bow-wave distance L/Y_{SB} (based on M_1) ahead of the blade leading edge is shown in figure 17(b). At low back pressure, the calculated bow wave was relatively close to the blade leading edge, being approximately 0.12 the distance between the upstream stagnation streamlines. As the back pressure increased, the bow wave moved away from the blade rather rapidly, being about 4.5 times the initial distance at the highest back pressure. The measured distance was obtained from the crystal data by extending the passage shock to the stagnation streamline. (At the highest back-pressure condition E, where the shock configuration seemed to vary from passage to passage and two limiting shock lines were established, the rearward shock position in figure 11 was used to determine the measured location of the bow wave.) Good agreement between the measured and the computed bow-wave distance from the blade leading edge was obtained.

The computed distance of the bow wave ahead of the leading edge was based on isolated-bow-wave theory, and thus the relative upstream Mach number M_1 was used to establish this distance. In a cascade of blades, the bow wave must exist in an expansion region of varying Mach number, as illustrated in figure 16. Another reference Mach number that could be obtained by iteration would be that existing at the point of intersection of the bow wave and the stagnation streamline. Therefore, the bow-wave distance from the blade was also computed with this reference Mach number

M_g and is shown in figure 17(b). For a given inlet condition, this distance is a function of the reference Mach number. At low back pressures the reference Mach number was lower than the relative inlet Mach number, and the bow-wave distance was greater than that obtained from M_1' ; whereas at high back pressure, M_g was greater than M_1' and the bow wave was therefore closer to the blade.

The two methods of establishing an effective Mach number ahead of the bow wave are the limits of the actual Mach number existing there. In the present investigation, the first method shows better agreement with the measured data than the second method. However, it is possible that another rotor would show a different correlation. It must be kept in mind that the measured distance was obtained by arbitrarily extending the crystal-probe data to the stagnation streamline.

The analytical methods (refs. 4 to 6) for approximating the location of the bow wave compare favorably with the observed shock-wave location, especially in the region of lower back pressure, for the rotor investigated.

Magnitude of bow-wave losses. - The methods used to calculate the location of the bow wave can also be extended to compute the shock loss in the bow wave. The bow wave is that part of the shock extending from the stagnation streamline ahead of the blade entrance region to infinity. The theory applied makes use of the fact that the losses suffered from all the bow waves between two blades are the same as the losses across one bow wave from the stagnation streamline to infinity. An outline of the calculation procedures based on the methods of references 4 to 6 is included in appendix B. The variation of the calculated bow-wave shock loss with operating conditions is shown in figure 18. As indicated in reference 1, at the low back pressures or low incidence angles, the loss coefficient in the bow wave was very small, being about 0.01. The loss coefficient associated with the bow wave increased gradually as the incidence angle increased, becoming approximately 0.04 at the highest back pressure. Thus, the calculated loss coefficient for the bow wave over the range of operation remained relatively low compared with the over-all loss coefficients usually obtained in the tip region of transonic-compressor rotors.

Discussion of Loss Variations

Also shown in figure 18 is the variation of computed passage shock loss with incidence angle, replotted from figure 14. The passage shock loss and the bow-wave shock loss were added together to indicate the over-all shock loss computed for the tip of this compressor rotor. The pseudo-tip-element loss coefficient is replotted (from fig. 14) in figure 18 for

comparison with the computed shock-loss coefficients. The bow wave contributed a small part of the over-all computed shock-loss coefficient. Thus, the comparison of the computed shock-loss coefficient and the measured loss coefficient is similar to that made in a previous section between passage shock and measured loss coefficients. The over-all shock-loss coefficient decreased as the incidence angle increased, whereas the measured loss coefficient increased. The reason for the difference in the trends of these loss coefficients is discussed in the next paragraph.

In reference 1, the qualitative variation of bow-wave, passage shock, and profile losses with rotor operating conditions is discussed. Profile losses are all losses other than shock losses. The results of the present investigation gave some quantitative value of the shock-loss variation. The experimental trend of the bow-wave loss was essentially that indicated in reference 1. The bow-wave loss obtained for this rotor was relatively small and did not contribute appreciably to the over-all loss variation. The passage-shock trends at high incidence angles could not be deduced in the reference because of the conflicting effects of incidence angle, Mach number magnitude, and shock location. The passage shock loss determined in the present investigation decreased with incidence angle above the rotor peak-efficiency condition. This decrease occurred because the shock moved forward in the blade passage at such a rate that the Mach number at the shock was decreased in spite of the increased incidence angle. Thus, the passage shock-loss variation depends on the rate of change of the shock location with incidence angle. These factors may depend to some extent on blade or rotor geometry.

The difference between the computed shock loss (passage shock plus bow wave) and the measured over-all loss has been termed a profile loss in reference 1. In figure 18, the shock loss was found to be a large part of the measured over-all loss in the region of rotor peak efficiency. References 1 and 2, which used different methods of estimating shock loss but considered rotor operation in the range of peak efficiency, also showed that the over-all pressure losses were largely shock losses.

As the incidence angle increased, the profile losses must have become larger, as indicated by the large differences between the computed shock loss and the measured over-all loss. This trend is in general agreement with the profile-loss variation deduced in reference 1. The results of the present investigation cannot indicate the reason for the large increase in profile loss. However, the increase in profile loss occurs in the presence of large subsonic diffusion and poor flow conditions resulting from a shock - boundary-layer interaction. Both these factors contribute to high profile losses. It can be stated from the results of this investigation that the variation in profile loss is the principal cause of the trend of increasing loss coefficient with incidence angle usually observed in transonic-compressor rotors.

SUMMARY OF RESULTS

The use of static-pressure crystal pickups over the rotor tip and the analysis possible with these data produced the following results:

1. The crystal static-pressure pickups indicated a large instantaneous static-pressure rise between the blade suction surface and pressure surface, which is indicative of a passage shock.
2. The passage shock location varied considerably with rotor operating conditions. At very low back pressures, the shock was oblique to the stream and fell behind the blade trailing-edge suction surface. As back pressure increased, the shock became essentially normal to the mean stream flow and then moved forward in the blade passage with a further increase in back pressure. At the highest back pressure, the shock stood a considerable distance ahead of the blade leading edge. This substantiates the analytical flow model presented in reference 1.
3. The computed passage shock-loss coefficient was rather high, being about 0.19 at the rotor maximum-efficiency condition. The maximum computed passage shock loss for this rotor was obtained near the point of rotor maximum efficiency.
4. The distance of the bow wave ahead of the blade leading edge varied considerably with operating conditions. At low back pressures, the bow wave was very close to the blade leading edge, standing ahead of the blade about 0.12 of the distance between the upstream stagnation streamlines. This distance increased almost 4.5 times at the point of highest back pressure. An analytically determined distance of the bow wave ahead of the blade leading edge agreed reasonably well with the measured distance.
5. The shock-loss coefficient associated with the bow wave was small (about 0.01) at the point of maximum efficiency and increased to approximately 0.05 at the point of highest back pressure.
6. At the point of rotor peak efficiency, the shock loss constituted a large portion of the over-all measured loss. However, at higher incidence angles, the increase in profile loss was the major factor in the large increase in rotor losses with incidence angle.

Lewis Flight Propulsion Laboratory
National Advisory Committee for Aeronautics
Cleveland, Ohio, January 27, 1958

APPENDIX A

SYMBOLS

- A area, sq ft
- A^*/A contraction ratio required to decelerate free stream to sonic velocity isentropically, $\frac{A^*}{A} = \frac{216 M}{(5+M^2)^3}$ for $\gamma = 1.4$
- a speed of sound, ft/sec
- B $(A^*/A)_1 (P'_1/P'_s)_c$
- C $\beta (\beta \tan \theta_s - \sqrt{\beta^2 \tan^2 \theta_s - 1})$
- c chord length, in.
- c' $c - 2r_{le}$
- D diffusion factor
- g intersection of bow wave with stagnation streamline
- g" intersection of suction surface with passage shock
- $\Delta H/U_t^2$ work coefficient
- h stagnation-streamline deflection, height of blade above stagnation streamline, in.
- i incidence angle, angle between relative inlet-air direction and tangent to blade mean camber line at leading edge, deg
- i_{ss} suction-surface incidence angle, angle between relative inlet-air direction and tangent to suction surface at blade leading edge, deg
- L distance of bow wave ahead of blade leading edge
- l point of intersection of any Mach line and stagnation streamline
- l_n distance along Mach line between suction surface and stagnation streamline, in.

M	Mach number
n	arbitrary point on blade suction surface
P	total pressure, lb/sq ft
p	static pressure, lb/sq ft
r_{le}	blade leading-edge radius, in.
s	blade spacing, in.
t	blade thickness, in.
V	air velocity, ft/sec
w	weight flow, lb/sec
x	component of coordinate system
x_o	distance from foremost point of detached shock to intercept of its asymptote on y-axis
Y_{SB}	distance between upstream stagnation streamlines, $s \cos \beta_1'$
y	component of coordinate system
α	angle between passage shock and chord, deg
β	$\sqrt{M^2 - 1}$
β_1'	relative inlet-air angle, angle between relative air velocity and axial direction, deg
γ	ratio of specific heats, 1.4
γ^o	blade-chord angle, angle between blade chord and axial direction, deg
η	angle between sonic line and normal to free-stream direction, deg
η_{ad}	adiabatic efficiency

θ	local inclination of detached shock relative to x-axis (Φ of ref. 4), deg
λ	angle of streamline relative to x-axis, deg
μ	Prandtl-Meyer Mach angle, $\arcsin 1/M$, deg
ν	Prandtl-Meyer expansion angle, deg
$\Delta\nu$	amount of supersonic turning, deg
ξ	angle between tangent to blade suction surface and chord, deg
ρ	density, lb/cu ft
τ	dimensionless height of blade above stagnation streamline, h/Y_{SB}
ϕ	camber angle, deg
$\phi_{ss}/2$	angle between chord and tangent to suction surface at blade leading edge, deg
$\bar{\omega}$	total-pressure-loss coefficient, over-all measured loss
$\bar{\omega}_{bs}$	total-pressure-loss coefficient, calculated bow-wave loss
$\bar{\omega}_{ps}$	total-pressure-loss coefficient, calculated passage shock loss
Subscripts:	
a	immediately before passage shock
b	immediately behind passage shock
c	centroid of stream tube passing sonic line
d	immediately behind bow-wave shock
g	conditions at intersection of shock and stagnation streamline
m.a.	mass-averaged value
n	arbitrary point on suction surface
n*	point on suction surface at which Mach number and flow direction equal upstream conditions

S sonic point of detached wave

SB sonic point of body

s conditions along sonic line

ss suction surface of blade

O stagnation conditions

1 upstream of rotor

2 downstream of rotor

Superscript:

' relative to rotor

APPENDIX B

METHODS OF COMPUTING INLET FLOW CONDITIONS AND SHOCK LOSSES

The methods of computing inlet flow conditions and shock losses are taken from reference 1. The flow model is shown in figure 19. The analysis of reference 1 was extended as follows:

(1) The flow conditions in the supersonic region are more completely described.

(2) The shock loss is evaluated when the passage shock shape and location are known.

(3) The stagnation streamlines in the supersonic region are calculated, so that the methods of references 4 and 5 can be used to establish analytically the distance of the shock ahead of the blade and the loss associated with the bow-wave part of the shock.

The following development can be adapted to any blade or cascade geometry. In this report, the method is applied to the circular-arc blade at the design condition of the transonic-compressor rotor of reference 3. The methods are applied in the same sense and have the same limitations as the usual blade-element approach.

Determination of Expansion Field

Figure 20 shows three flow conditions: (a) i_{ss} equal to zero; (b) i_{ss} greater than zero; and (c) i_{ss} less than zero. For an ideal expansion about the blade, there will be some point designated as n^* , at which the Mach number M_{n^*} and the direction of flow ξ_{n^*} will equal the upstream conditions. Then $M_{n^*}' = M_1'$, and $\xi_{n^*}' = \beta_1' - \gamma^0 = \phi_{ss}/2 + i_{ss}$. The expansion angle ν_{n^*} and the Mach angle μ_{n^*} can be found from the Mach number M_{n^*}' and the tables of reference 7. For a given blade geometry, the slope of the suction surface at any point with respect to the chord can be found, and the point at which the slope is equal to $\tan \xi_{n^*}$ is the desired point, n^* .

In figure 20(a), the flow enters the passage in a direction parallel to the suction surface at the blade leading edge; that is, $i_{ss} = 0$. The angle ξ_{n^*} is then equal to $\phi_{ss}/2$. For blades with a circular-arc suction surface,

$$\frac{\phi_{ss}}{2} = 2 \arctan \left(\frac{1 - \cos \phi/2}{\sin \phi/2} + \frac{t_{max} - 2r_{le}}{c'} \right) \quad (1)$$

where

$$c' = c - 2r_{le} \quad (2)$$

To find conditions at some other point, n , along the suction surface:

- (1) Choose a convenient increment of turning, Δv .
- (2) Find the direction of flow,

$$\tan \xi_n = \tan(\xi_{n*} - \Delta v) = \tan(\beta_1' - \gamma^0 - \Delta v)$$

(3) Determine the position of n on the suction surface by finding the point at which the slope of the surface is equal to $\tan \xi_n$.

(4) Determine the expansion to n , $v_n = v_{n*} + \Delta v$.

(5) Determine M_n from v_n and the tables of reference 7.

(6) Determine the Mach angle μ_n from M_n and the tables of reference 7.

(7) Determine the Mach line from coordinates of n and the angle between the Mach line and the chord, $(\xi_n + \mu_n)$.

The expansion around the leading-edge circle is found by the same steps starting at n^* , but the increment of turning Δv must be taken as negative.

Figure 20(b) shows a condition of positive i_{ss} . The point on the blade at which the conditions are the same as the upstream conditions is actually some point on the leading-edge circle. As before, the Mach number M_{n*}' equals M_1' and the flow angle ξ_{n*} can be found from β_1' and the geometry,

$$\xi_{n*} = \beta_1' - \gamma^0 = \frac{\phi_{ss}}{2} + i_{ss}$$

To find the flow at another point:

- (1) Choose Δv .
- (2) $\xi_n = \xi_{n*} - \Delta v = \beta_1' - \gamma^0 - \Delta v$.

- (3) Determine the position of n .
- (4) Determine v_n .
- (5) Determine M_n .
- (6) Determine μ_n .
- (7) Determine the Mach line.

The expansion fan ahead of the line along which M equals M_1' can be found by taking negative values of Δv .

Figure 20(c) shows a negative i_{ss} . For this condition the point on the blade surface at which the flow conditions are equal to upstream conditions is downstream of the leading edge. The expansion field for this case can also be found by the foregoing methods.

Thus, for given upstream conditions and blade geometry, the flow conditions can be analytically determined indirectly for any point in the expansion region. It should be noted that this theory is not valid beyond the passage shock.

Determination of Stagnation Streamline

The stagnation streamline ahead of the passage shock can be found by applying a continuity relation to the expansion field already determined. The upstream weight flow per unit height per blade passage (see fig. 20(a)) can be written

$$w = (\rho VA)_1 = (\rho M' a s \cos \beta')_1 \quad (3)$$

The weight flow crossing an expansion line is

$$w = (\rho VA)_n = (\rho M' a l \sin \mu)_n$$

where l_n is the length of the line from n to l . Since $M_n' \sin \mu_n = 1.0$ by definition in Prandtl-Meyer expansion theory, the weight-flow term can be simplified to

$$w = (\rho a l)_n \quad (4)$$

Equating the upstream weight flow to that in the expansion field gives

$$(\rho M' a s \cos \beta')_1 = (\rho a l)_n$$

and dividing both sides by $(\rho'_0 a'_0)_1$ gives

$$\left(\frac{\rho'}{\rho'_0} \frac{a'}{a'_0} M' s \cos \beta' \right)_1 = \left(\frac{\rho'}{\rho'_0} \frac{a'}{a'_0} l \right)_n \frac{(\rho'_0 a'_0)_n}{(\rho'_0 a'_0)_1}$$

Since $T'_1 = T'_n$, $a'_{0,n}/a'_{0,1} = 1.0$, and the density ratio can be written

$$\frac{\rho'_{0,n}}{\rho'_{0,1}} = \frac{P'_a}{P'_1}$$

then

$$\left(\frac{\rho'}{\rho'_0} \frac{a'}{a'_0} M' s \cos \beta' \right)_1 = \left(\frac{\rho'}{\rho'_0} \frac{a'}{a'_0} l \right)_n \frac{P'_a}{P'_1} \quad (5)$$

The term P'_a/P'_1 represents the pressure ratio across the bow wave. For this investigation an initial value of 1.0 was assigned to the term P'_a/P'_1 . The next section, which deals with bow-wave loss, shows this assumption to be within the accuracy of these calculations, and therefore no correction for total-pressure loss across the bow wave was made.

The left side of equation (5) is a function of upstream flow conditions and blade spacing. The density and velocity terms on the right side of equation (5) are functions of the Mach number along the expansion line under consideration. Since $P'_a/P'_1 = 1.0$, equation (5) can be solved for l_n :

$$l_n = \frac{\left(\frac{\rho'}{\rho'_0} \frac{a'}{a'_0} M' s \cos \beta' \right)_1}{\left(\frac{\rho'}{\rho'_0} \frac{a'}{a'_0} \right)_n} \quad (6)$$

By combining l_n with the Mach angle, the direction of flow, and the coordinates of n as found in the section Determination of Expansion Field, the coordinates of the point l where the Mach line intersects the stagnation streamline can be determined.

Application of these steps to a series of Mach lines will analytically approximate the stagnation streamline between the bow wave and the passage shock.

Determination of Shock Loss

The flow model for calculating the total-pressure-loss coefficient is shown in figure 21. The total-pressure ratio across the shock was

computed and mass-averaged by the methods of reference 2, and the loss coefficient was computed from the mass-averaged total-pressure ratio. The expansion field and the stagnation streamline were computed for the given flow condition and geometry according to the methods previously described. The shock line was assumed to consist of a series of straight lines connecting the shock points indicated by the crystal pickups. The shock upstream of the first crystal point was drawn normal to the stagnation streamline and through the point. Between the last crystal point that showed a static-pressure rise and the suction surface, the shock was taken as an extension of the straight line determined by the previous two crystal lines.

Then for each point of intersection of a Mach line and the shock, the shock loss is determined by the following steps:

(1) Determine the angle α between the chord and the shock line. This angle may change across the passage.

(2) Determine the component of the Mach number M'_n normal to the shock:

$$M'_{n,\text{normal}} = M'_n \sin(\xi_n + \alpha)$$

where ξ_n is measured from the chord to the direction of flow.

(3) Determine the total-pressure ratio P'_b/P'_a from $M'_{n,\text{normal}}$ and the tables of reference 7.

$$(4) \left(\frac{w}{\rho'_0 a'_0} \frac{P'_b}{P'_a} \right)_{\text{m.a.}} = \sum_{y_n=y_{g''}}^{y_g} \left(M' \frac{\rho}{\rho_0} \frac{a}{a_0} \right)_n \sin(\xi_n + \alpha) \frac{P'_b}{P'_a} \frac{\Delta y}{\sin \alpha}$$

where y is measured perpendicular to the chord.

$$(5) \left(\frac{w}{\rho'_0 a'_0} \right)_{\text{m.a.}} = \sum_{y_n=y_{g''}}^{y_g} \left(M' \frac{\rho}{\rho_0} \frac{a}{a_0} \right)_n \sin(\xi_n + \alpha) \frac{\Delta y}{\sin \alpha}$$

$$(6) \left(\frac{P'_b}{P'_a} \right)_{\text{m.a.}} = \frac{\left(\frac{w}{\rho'_0 a'_0} \frac{P'_b}{P'_a} \right)_{\text{m.a.}}}{\left(\frac{w}{\rho'_0 a'_0} \right)_{\text{m.a.}}}$$

$$(7) \quad (\bar{\omega}_{ps})_{m.a.} = \frac{1 - \left(\frac{P'_b}{P'_a}\right)_{m.a.}}{1 - \left(\frac{p}{P'_r}\right)_1}$$

The parameter $\bar{\omega}_{ps}$ is a mass-averaged total-pressure-loss coefficient based on an assumed Mach number variation along the face of the shock.

Determination of Bow-Wave Location by Analytical Method

References 4 and 5 developed an approximate method of predicting the location of detached shock waves for given upstream conditions. Reference 5 extended the method to find bow-wave loss in a supersonic blade row. The present analysis is a modification of the previous work to establish the location of the shock in the blade passage.

Figure 22 shows the modified flow model. The model is oriented so that the direction of free-stream flow is along the x-axis, and the y-coordinate is measured from the preceding blade. The coordinate y_g is the stagnation streamline, which is drawn as a straight line in the direction of flow. For circular-arc blades the stagnation streamline has some curvature, but this curvature is small and the assumption of a straight line should be reasonable, particularly for cases where the bow wave stands near the nose. Since the nose of the blade is small, the sonic point on the blade SB can be considered at the nose for all practical purposes. Thus, the distance L is measured from the nose to the intersection of the bow wave and the stagnation streamline.

By assuming the bow wave to be a hyperbola asymptotic to a Mach line and using Y_{SB} as a reference dimension, an equation for the bow wave can be written

$$\left(\frac{x}{Y_{SB}}\right)^2 - \beta^2 \left(\frac{y}{Y_{SB}} - \frac{y_g}{Y_{SB}}\right)^2 = \left(\frac{x_0}{Y_{SB}}\right)^2 \quad (7)$$

where β is the cotangent of the Mach angle and x_0 is the distance from the vertex of the bow wave to the intersection of its asymptotes.

The angle between the stream direction and the tangent to the shock at any point is obtained from

$$\frac{dy}{dx} = \tan \theta = \frac{\frac{x}{Y_{SB}}}{\beta \sqrt{\left(\frac{x}{Y_{SB}}\right)^2 - \left(\frac{x_0}{Y_{SB}}\right)^2}} = \frac{\sqrt{\left(\frac{x_0}{Y_{SB}}\right)^2 + \beta^2 \left(\frac{y}{Y_{SB}} - \frac{y_g}{Y_{SB}}\right)^2}}{\beta^2 \left(\frac{y}{Y_{SB}} - \frac{y_g}{Y_{SB}}\right)} \quad (8)$$

The location of S is

$$\frac{y_S}{y_{SB}} = \frac{\left(\frac{x_O}{y_{SB}}\right) \cot \theta_S}{\beta \sqrt{\beta^2 - \cot^2 \theta_S}} + \frac{y_g}{y_{SB}} \quad (9)$$

$$\frac{x_S}{y_{SB}} = \frac{\beta \left(\frac{x_O}{y_{SB}}\right)}{\sqrt{\beta^2 - \cot^2 \theta_S}} \quad (10)$$

where, for $\gamma = 1.4$,

$$\theta_S = \arcsin \left[\frac{1}{M'} \sqrt{\frac{3M'^2 - 2}{7}} + \sqrt{\left(\frac{3M'^2 - 2}{7}\right)^2 + \frac{5}{7}} \right] \quad (11)$$

Values of θ_S are obtained from reference 7. From equation (9),

$$\frac{x_O}{y_{SB}} = \beta \left(\frac{y_S}{y_{SB}} - \frac{y_g}{y_{SB}} \right) \sqrt{\beta^2 \tan^2 \theta_S - 1} \quad (12)$$

The dimensionless distance from the foremost point of the shock to the x-coordinate of the body sonic point is

$$\frac{L}{y_{SB}} = \frac{x_{SB}}{y_{SB}} - \frac{x_O}{y_{SB}} \quad (13)$$

where, from figure 22,

$$\frac{x_{SB}}{y_{SB}} = \frac{x_S}{y_{SB}} + \left(\frac{y_S}{y_{SB}} - 1 \right) \tan \eta \quad (14)$$

If equations (10), (12), (13), and (14) are combined to eliminate all unknown coordinates except y_S/y_{SB} and L/y_{SB} , equation (13) becomes

$$\frac{L}{y_{SB}} = \frac{y_S}{y_{SB}} (C + \tan \eta) - \tan \eta - C \frac{y_g}{y_{SB}} \quad (15)$$

where

$$C = \beta \left(\beta \tan \theta_S - \sqrt{\beta^2 \tan^2 \theta_S - 1} \right) \quad (16)$$

As in reference 4, the quantity y/Y_{SB} is determined by applying a continuity relation across the sonic line. An average stagnation pressure behind the sonic line is associated with the streamline that represents the mass centroid of the fluid passing the sonic line. Since the stagnation pressure along such a streamline does not change between the bow wave and the sonic line, the desired pressure can be found for the point at which the centroid streamline crosses the bow wave. This point y_c is

$$y_c = \frac{y_S + y_G}{2} \quad (17)$$

Then, from equations (8), (12), and (17),

$$\begin{aligned} \tan \theta_c &= \frac{\sqrt{\left(\frac{x_O}{Y_{SB}}\right)^2 + \beta^2 \left(\frac{y_c}{Y_{SB}} - \frac{y_G}{Y_{SB}}\right)^2}}{\beta^2 \left(\frac{y_c}{Y_{SB}} - \frac{y_G}{Y_{SB}}\right)} \\ &= \frac{1}{\beta} \sqrt{1 + 4(\beta^2 \tan^2 \theta_S - 1)} \end{aligned} \quad (18)$$

The Mach number at this point is

$$M'_c = M' \sin \theta_c \quad (19)$$

The total-pressure ratio can be found from M'_c and the normal-shock tables of reference 7 where, for $\gamma = 1.4$,

$$\left(\frac{P'_S}{P'_1}\right)_c = \left(\frac{6M'^2_c}{M'^2_c + 5}\right)^{7/2} \left(\frac{6}{7M'^2_c - 1}\right)^{5/2} \quad (20)$$

The continuity relation gives

$$\frac{A_S}{A_1} = \frac{\rho_1 V_1}{(\rho_S V_S)_c} = \left(\frac{P'_1}{P'_S}\right)_c \left[\frac{\rho_0 V_0}{(\rho V)_{cr}}\right] = \left(\frac{P'_1}{P'_S}\right)_c \left(\frac{A^*}{A}\right)_1 \quad (21)$$

where $(A^*/A)_1$ is the contraction ratio required to decelerate the free stream to sonic velocity isentropically. For $\gamma = 1.4$,

$$\left(\frac{A^*}{A}\right)_1 = \frac{216 M'}{[5 + (M')^2]^3} \quad (22)$$

From figure 22,

$$\frac{A_S}{A_1} = \frac{y_S - Y_{SB}}{(y_S - y_g) \cos \eta} = \left(\frac{P_1}{P_S} \right)_c \left(\frac{A^*}{A} \right)_1 = B \quad (23)$$

Then

$$\frac{y_S}{Y_{SB}} = \frac{1 - B \cos \eta \frac{y_g}{Y_{SB}}}{1 - B \cos \eta} \quad (24)$$

The value of η is close to λ_S and is assumed equal to it; then

$$\eta = \lambda_S = \arctan \frac{5 \cot \theta_S (M_1^2 \sin^2 \theta_S - 1)}{5 + M_1^2 (6 - 5 \sin^2 \theta_S)} \quad (25)$$

Combining equations (24) and (25) with equation (15) gives

$$\frac{L}{Y_{SB}} = \left(1 - \frac{y_g}{Y_{SB}} \right) \left(\frac{C + B \sin \lambda_S}{1 - B \cos \lambda_S} \right) \quad (26)$$

$$= \tau \left(\frac{C + B \sin \lambda_S}{1 - B \cos \lambda_S} \right) \quad (27)$$

This development states that the distance between the leading edge of the blade and the bow wave is a function of the upstream Mach number and the parameter τ , which is defined as $\left(1 - \frac{y_g}{Y_{SB}} \right)$. In this investigation τ was taken as the value h/Y_{SB} , where h is the normal distance from the leading edge of the blade to the stagnation streamline. (The stagnation streamline must be extended beyond the shock in order to find h).

This method is based on a theory for isolated bodies for which the upstream Mach number is a constant. For a blade row the Mach number ahead of the bow wave varies. For this investigation two solutions were obtained by: (1) using the Mach number upstream of the rotor, that is, M_1 ; and (2) using the Mach number at the intersection of the bow wave and the stagnation streamline, that is, M_g . The second solution is an iterative process requiring an initial assumption of M_g . The distance L may then be calculated. If the Mach number at the intersection of the bow wave and the stagnation streamline is found from conditions along the stagnation streamline, a new approximation to the Mach number is obtained. This procedure is repeated until the assumed Mach number equals that at the intersection of the bow wave and the stagnation streamline.

The following steps are necessary to find $L/Y_{SB} = f(M', \tau)$:

(1) For a given M' :

- (a) Find β from $\beta = \sqrt{(M')^2 - 1}$.
- (b) Find θ_S from equation (11).
- (c) Find λ_S from equation (25).
- (d) Find C from equation (16).
- (e) Find $\tan \theta_c$ from equation (18).
- (f) Find M'_c from equation (19).
- (g) Find $(P'_g/P'_1)_c$ from equation (20).
- (h) Find $(A^*/A)_1$ from equation (22).
- (i) Find B from equation (23).
- (j) Find $\frac{1}{\tau} \frac{L}{Y_{SB}}$ from equation (27).

(2) For a given τ , find L/Y_{SB} . A plot of $L/\tau Y_{SB}$ against M is given in figure 23.

Determination of Bow-Wave Loss

Reference 5 presents a method for calculating the approximate losses across the bow-wave part of the shock. A model similar to that used in reference 5 is shown in figure 24 with the notation changed to that of the present report. As described in reference 5, the flow entering the blade passages 1-2 incurs shock losses across the bow-wave portions 1-2, 2'-3', 3"-4", and so forth. Since the section 2'-3' is identical to 2-3, the section 3"-4" is identical to 3-4, and so forth, the bow-wave loss is identical to the total loss suffered across the portions 1-2, 2-3, 3-4, and so forth. Therefore, the total loss across the bow wave can be found by considering one bow wave from its origin (the stagnation streamline) to infinity. This method uses all the assumptions previously made, including the hyperbolic shock-wave form. The equations from reference 5 are given here for completeness.

The total-pressure loss is expressed

$$1 - \frac{P'_a}{P'_1} = \tau \int_{y_g/\tau Y_{SB}}^{y_\infty/\tau Y_{SB}} \left(1 - \frac{P'_d}{P'_1}\right) d\left(\frac{y}{\tau Y_{SB}} - \frac{y_g}{\tau Y_{SB}}\right) \quad (28)$$

where y is taken perpendicular to the direction of flow.

The total-pressure recovery over a shock wave of given slope and Mach number is given by

$$\frac{P'_d}{P'_1} = \left[\left(\frac{2\gamma}{\gamma+1} \right) (M_1'^2 \sin^2 \theta) - \left(\frac{\gamma-1}{\gamma+1} \right) \right]^{1-\gamma} \left[\frac{(\gamma-1)M_1'^2 \sin^2 \theta + 2}{(\gamma+1)M_1'^2 \sin^2 \theta} \right]^{\frac{\gamma}{1-\gamma}} \quad (29)$$

Since the wave shape has been assumed to be hyperbolic, the angle of the wave can be written (see fig. 22)

$$\theta = \arctan \frac{\sqrt{\left(\frac{x_o}{\tau Y_{SB}}\right)^2 + \beta^2 \left(\frac{y}{\tau Y_{SB}} - \frac{y_g}{\tau Y_{SB}}\right)^2}}{\beta^2 \left(\frac{y}{\tau Y_{SB}} - \frac{y_g}{\tau Y_{SB}}\right)} \quad (30)$$

where $y/\tau Y_{SB}$ is measured perpendicular to the free-stream direction, and $x_o/\tau Y_{SB}$ is a constant that locates the hyperbola with respect to the leading edge.

The constant $x_o/\tau Y_{SB}$ was determined in the previous section and can be used with equations (29) and (30) to evaluate the integral of equation (28). The integral then becomes a function of only the upstream Mach number. The evaluation of the integral is given in reference 6 and is reproduced in figure 25 to aid in calculation.

In order to compare bow-wave losses with the other loss factors, the total-pressure loss is converted to a total-pressure-loss coefficient

$$C_{bs} = \frac{1 - \frac{P'_a}{P'_1}}{1 - \left(\frac{P}{P'}\right)_1}$$

REFERENCES

1. Schwenk, Francis C., Lewis, George W., and Hartmann, Melvin J.: A Preliminary Analysis of the Magnitude of Shock Losses in Transonic Compressors. NACA RM E57A30, 1957.
2. Lewis, George W., Tysl, Edward R., and Fessler, Theodore E.: Analysis of Transonic Rotor-Blade Passage Loss with Hot-Wire Anemometers. NACA RM E58C04, 1958.
3. Creagh, John W. R.: Performance Characteristics of an Axial-Flow Transonic Compressor Operating Up to Tip Relative Inlet Mach Number of 1.34. NACA RM E56D27, 1956.
4. Moeckel, W. E.: Approximate Method for Predicting Form and Location of Detached Shock Waves Ahead of Plane or Axially Symmetrical Bodies. NACA TN 1921, 1949.
5. Klapproth, John F.: Approximate Relative-Total-Pressure Losses of an Infinite Cascade of Supersonic Blades with Finite Leading-Edge Thickness. NACA RM E9L21, 1950.
6. Graham, Robert C., Klapproth, John F., and Barina, Frank J.: Investigation of Off-Design Performance of Shock-in-Rotor Type Supersonic Blading. NACA RM E51C22, 1951.
7. Ames Research Staff: Equations, Tables, and Charts for Compressible Flow. NACA Rep. 1135, 1953. (Supersedes NACA TN 1428.)



C-39136

Figure 1. - Transonic-compressor rotor designed for tip speed of 1300 feet per second.

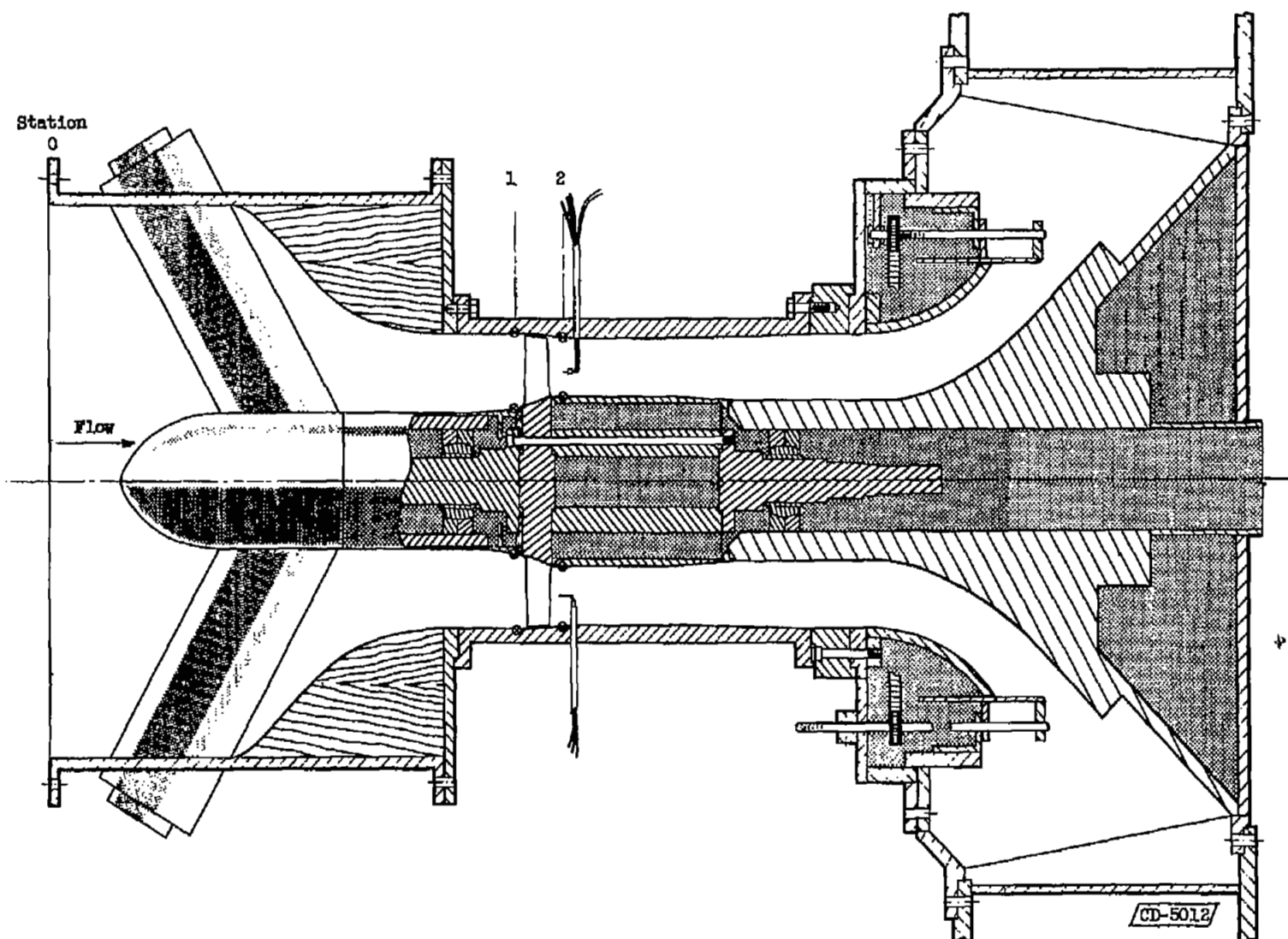
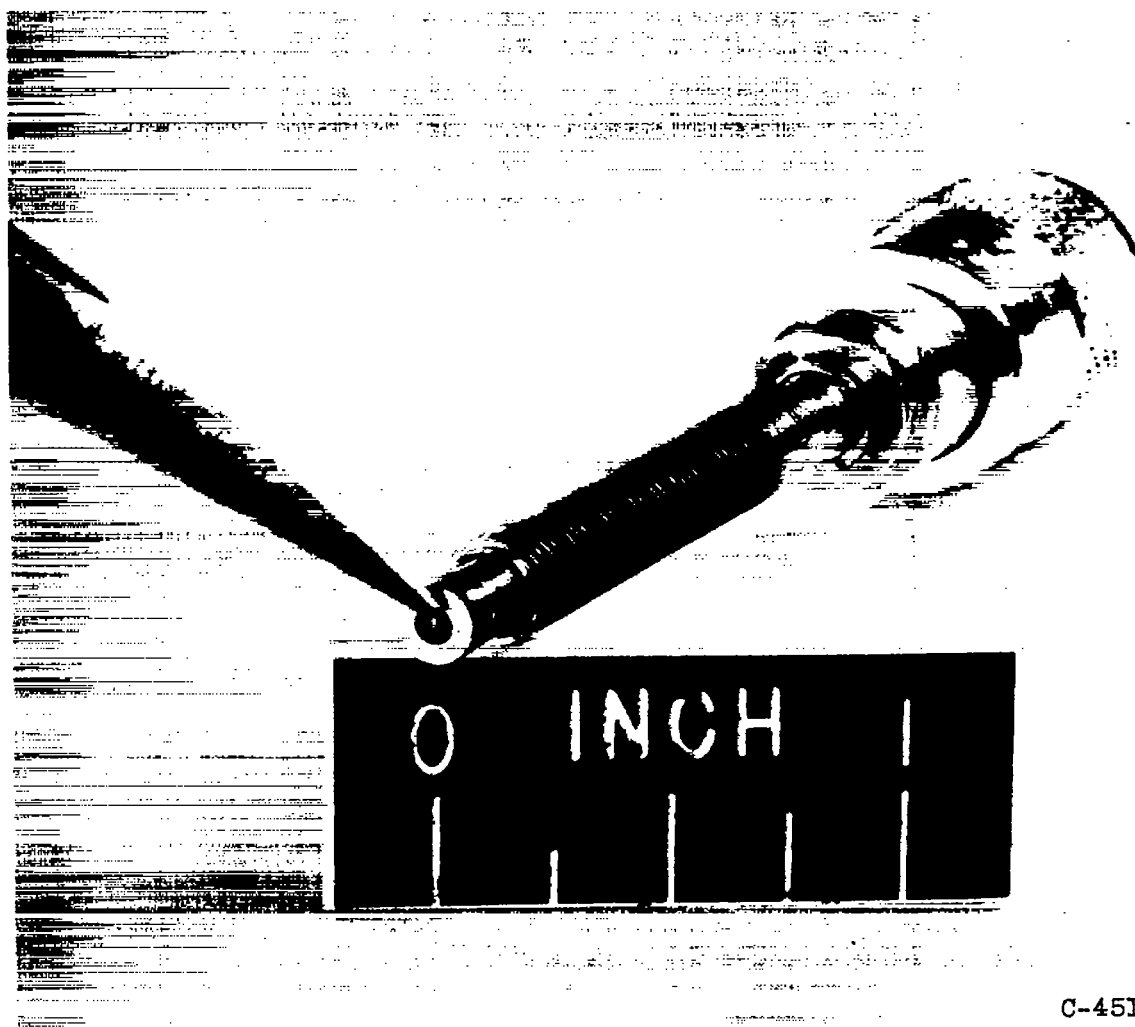


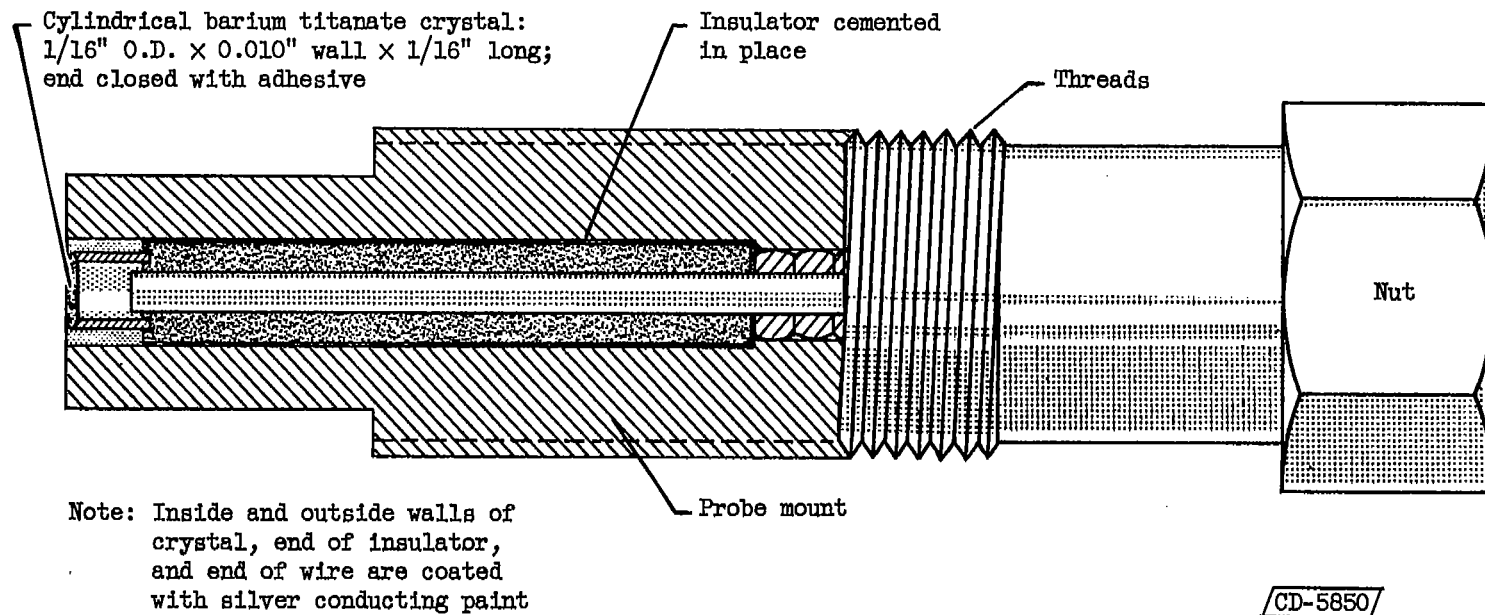
Figure 2. - Transonic-compressor installation.



C-45160

(a) Photograph.

Figure 3. - Barium titanate crystal probe used as static-pressure pickup.



(b) Cross-sectional diagram.

Figure 3. - Concluded. Barium titanate crystal probe used as static-pressure pickup.

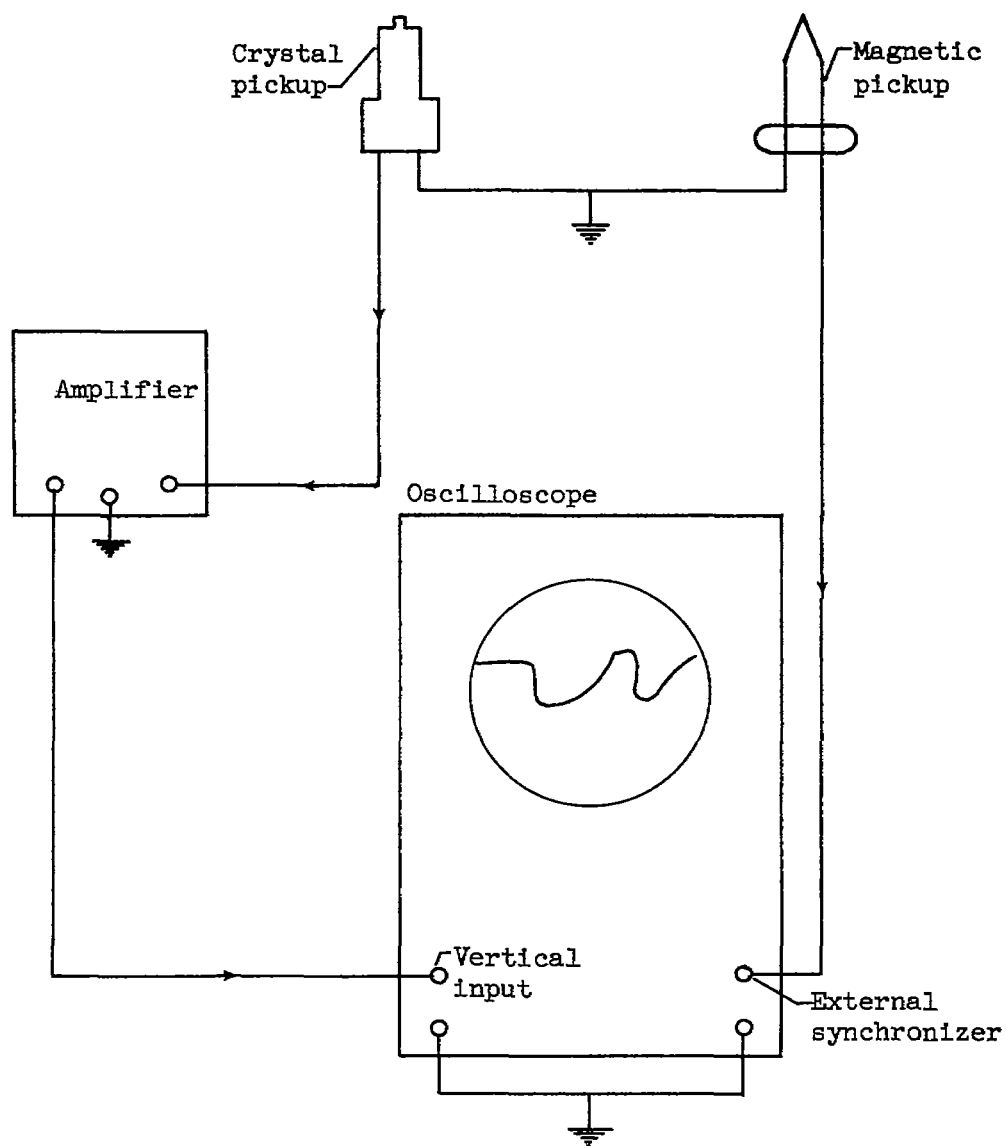


Figure 4. - Circuit diagram for indicating static-pressure variations on oscilloscope screen from barium titanate crystal probes.

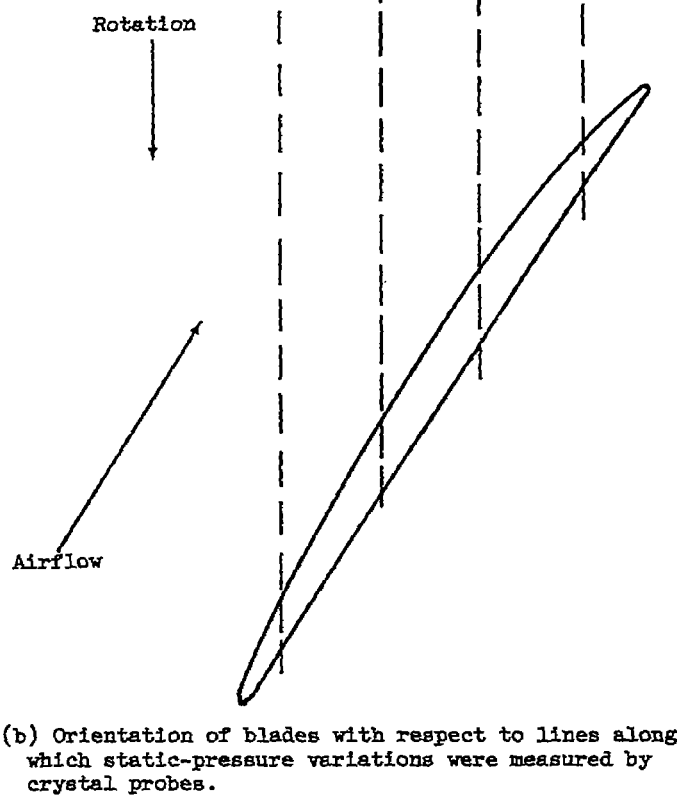
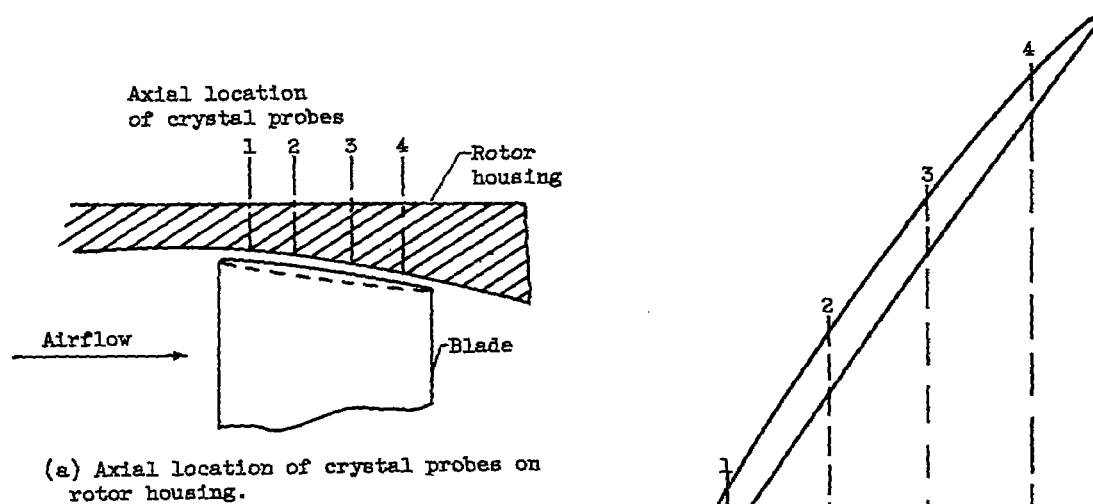


Figure 5. - Location of barium titanate crystal probes for indicating static-pressure variations at blade tip.

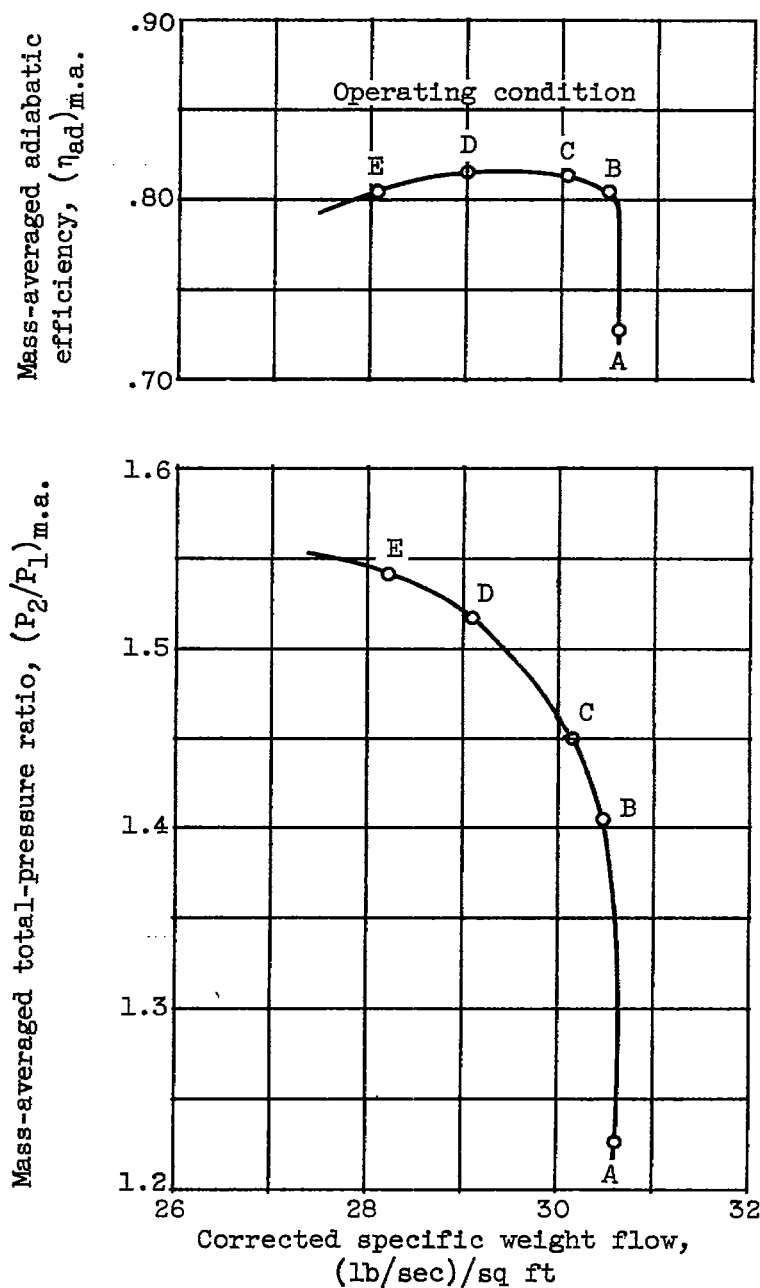


Figure 6. - Over-all performance of transonic-compressor rotor at design speed of 1300 feet per second. (Data from ref. 3.)

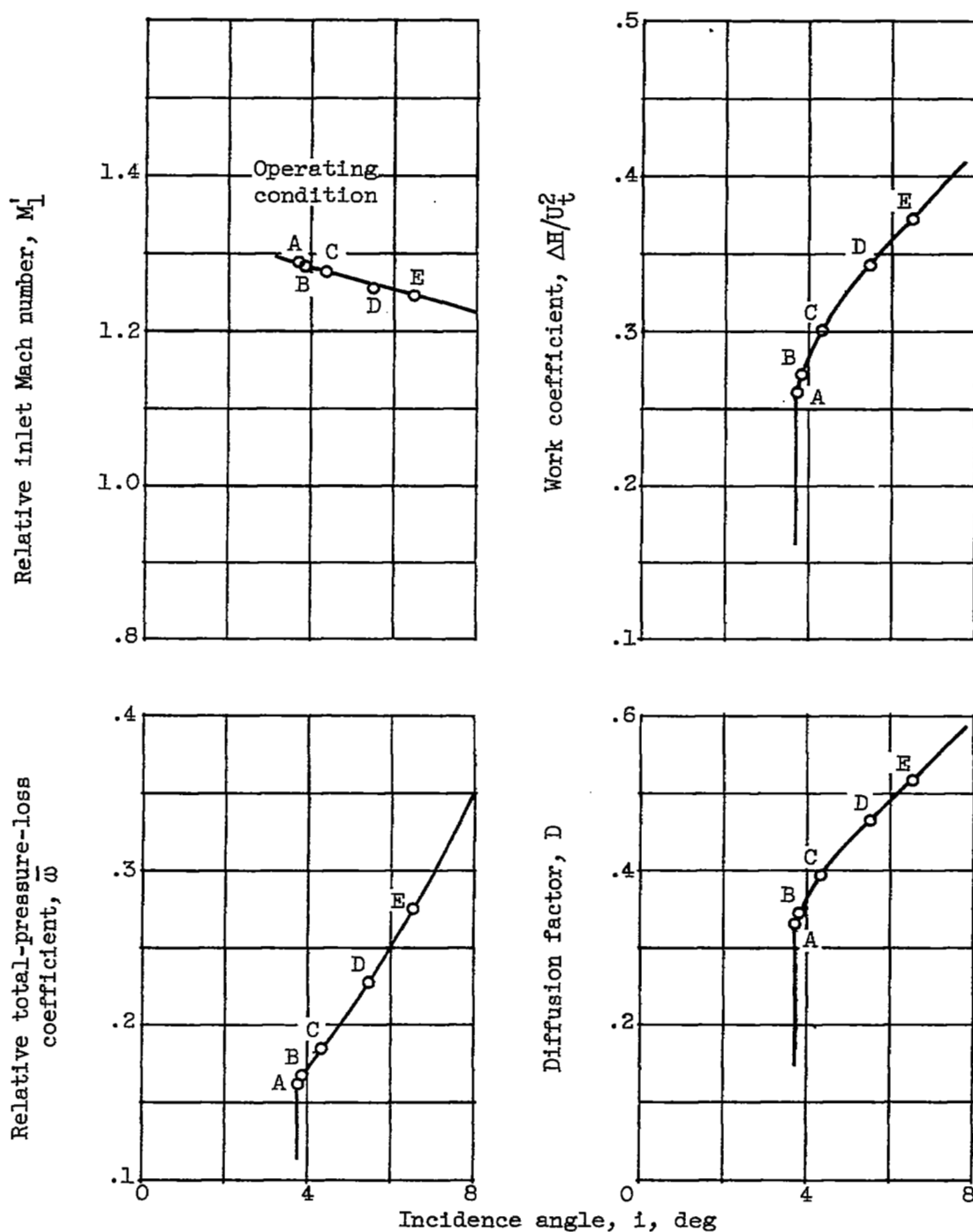


Figure 7. - Blade-element characteristics at 11 percent of annulus height from outer wall of transonic-compressor rotor at design speed. (Performance curves from ref. 3.)

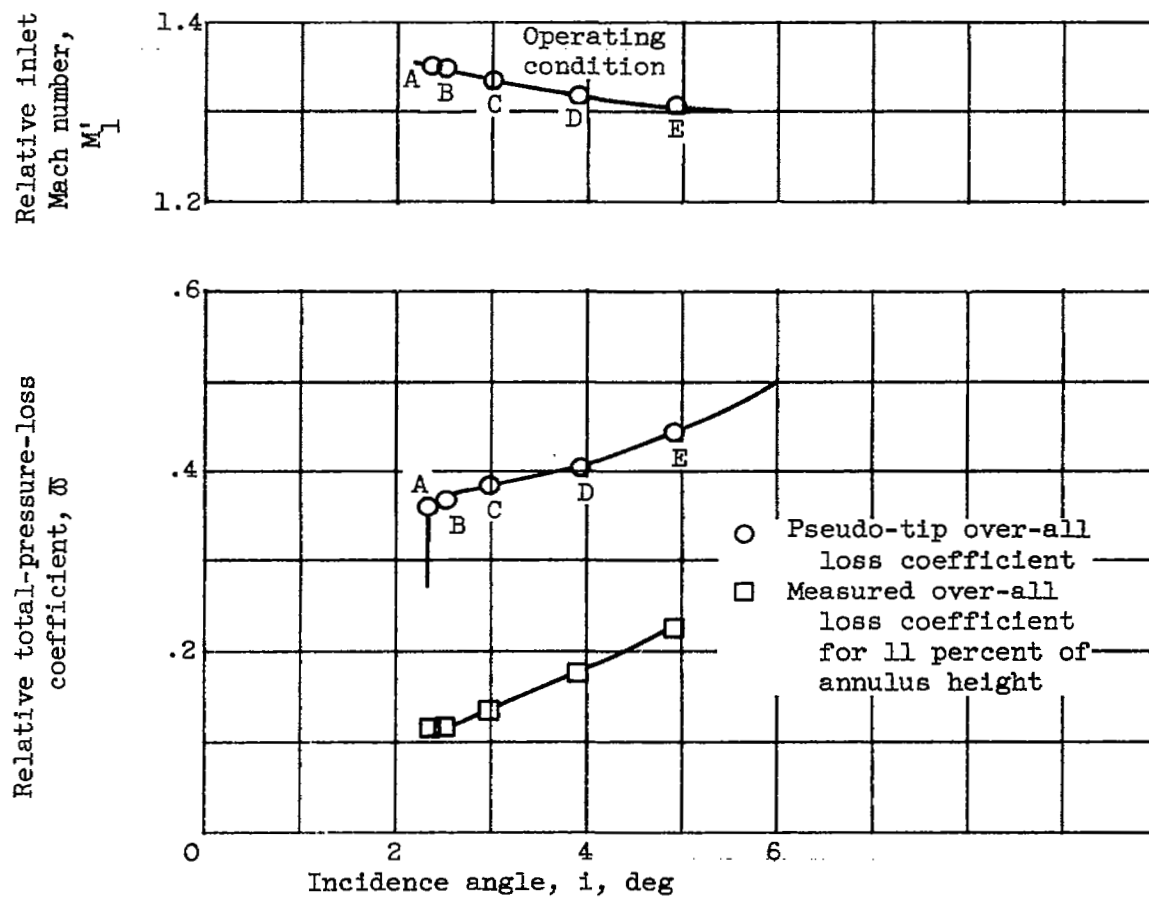
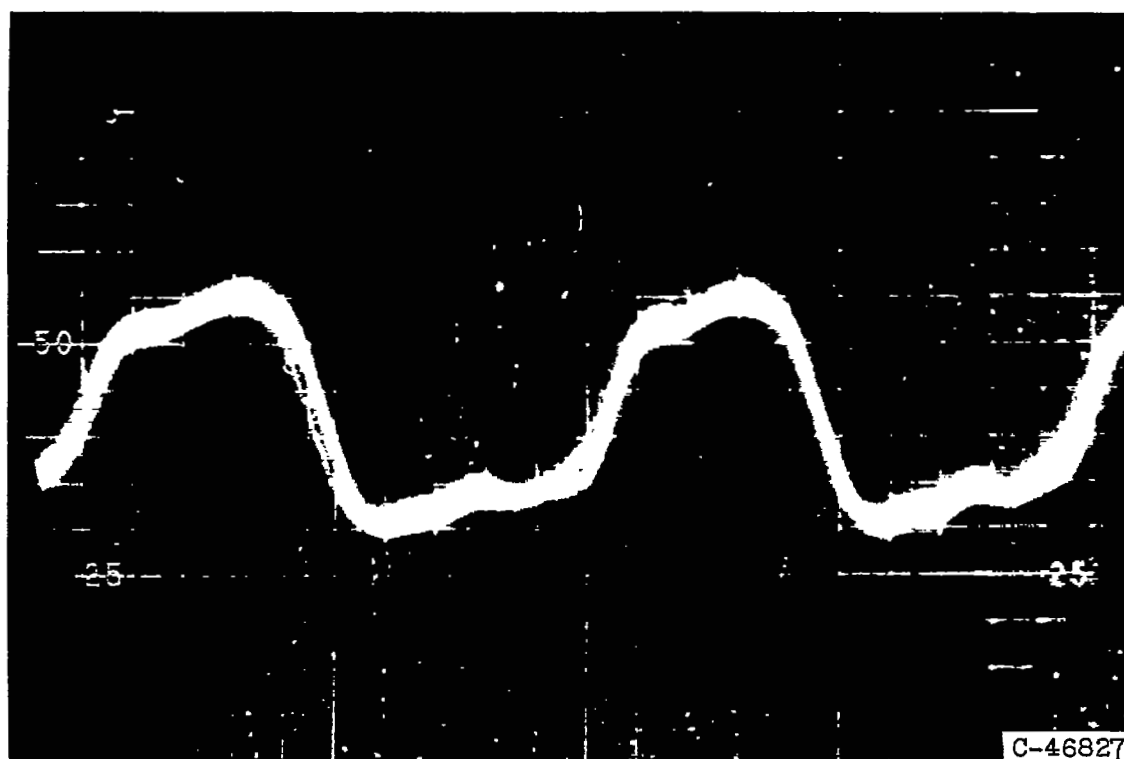


Figure 8. - Blade-element characteristics from reference 3 extrapolated to blade tip for comparison with crystal data.



Blade → | ←
 |
 Suction
 surface
 ↑
 Shock
 location
 ↓
 Pressure
 surface
← | ← Blade

Figure 9. - Oscilloscope screen showing typical trace of static-pressure variation at blade tip.

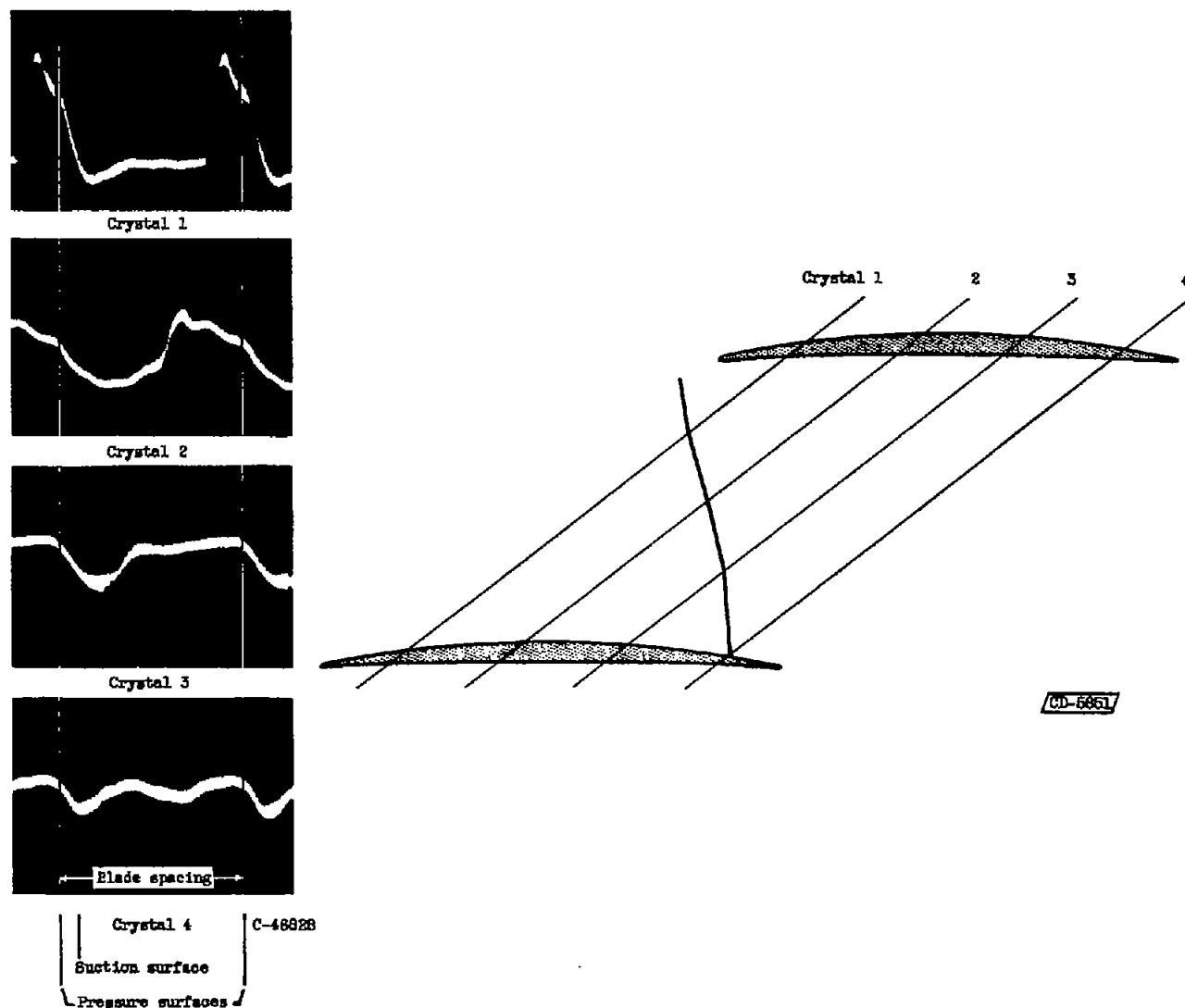
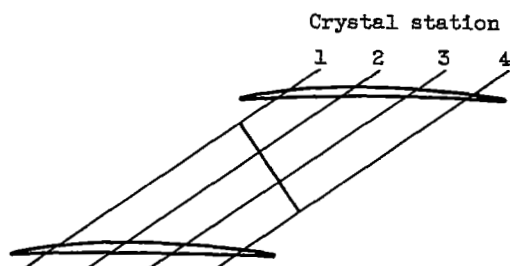
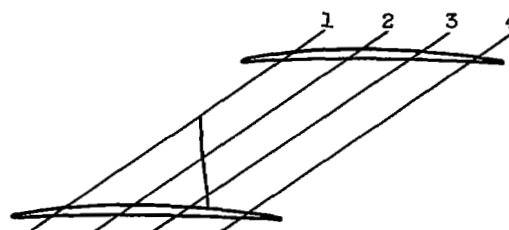


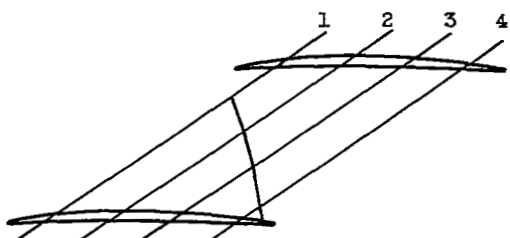
Figure 10. - Oscilloscope traces taken at the four crystal-probe stations and used to locate shock pattern in transonic rotor operating at design speed near maximum efficiency (point C of fig. 8).



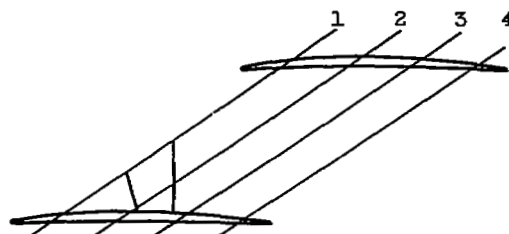
(a) Operating condition A.



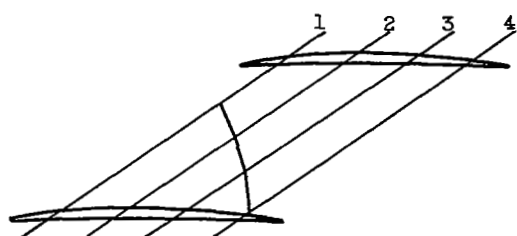
(d) Operating condition D.



(b) Operating condition B.



(e) Operating condition E.



(c) Operating condition C.

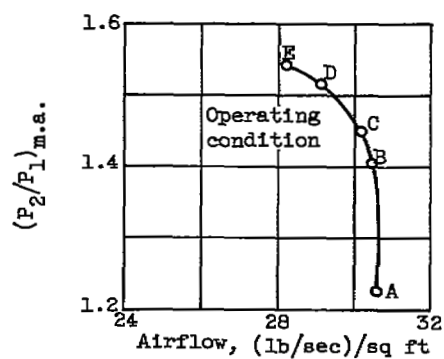


Figure 11. - Effect of operating conditions on shock configurations as shown by crystal probes.

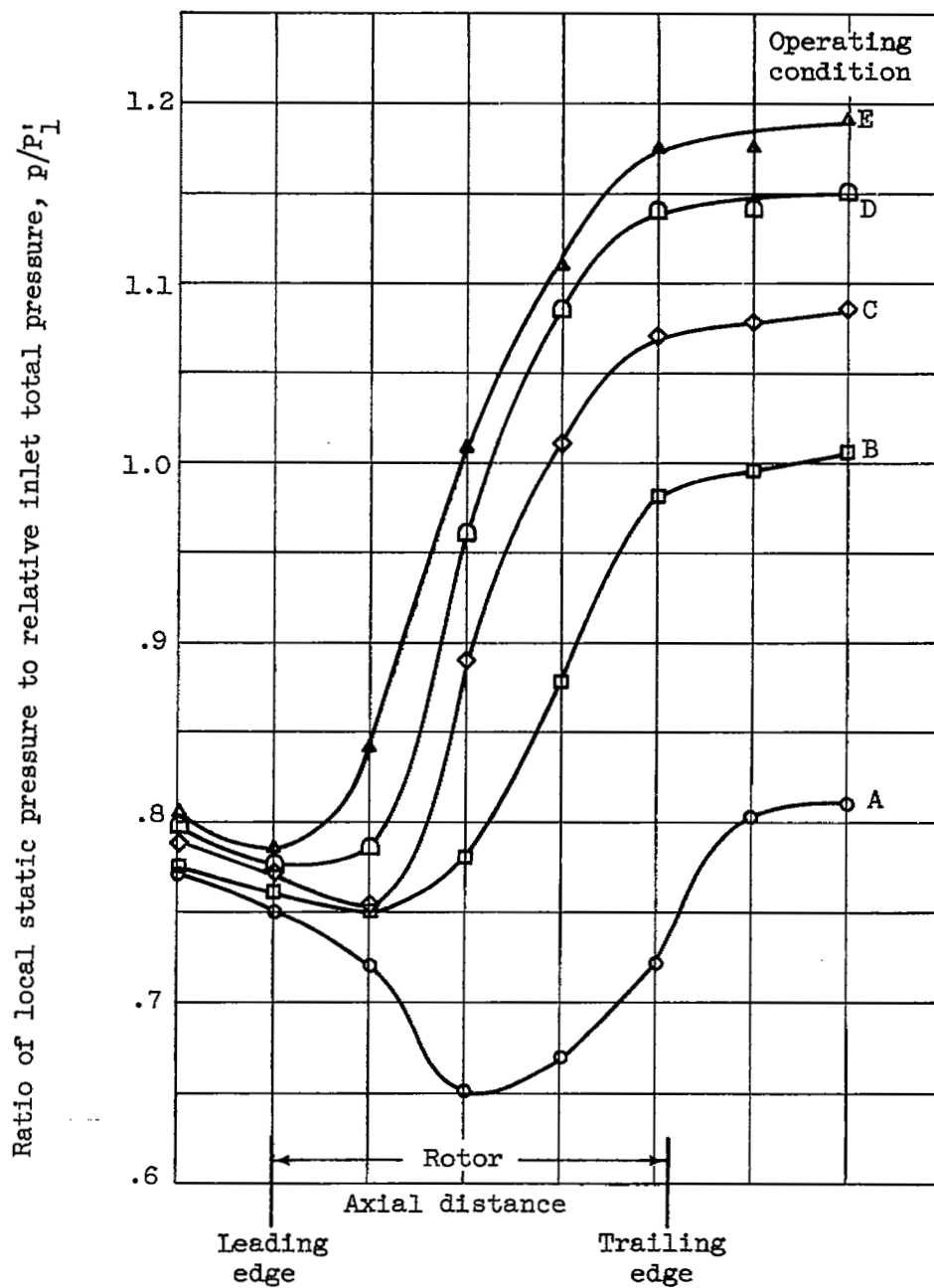


Figure 12. - Variation in static pressure measured by static-pressure taps in outer wall of transonic-compressor rotor at design speed.

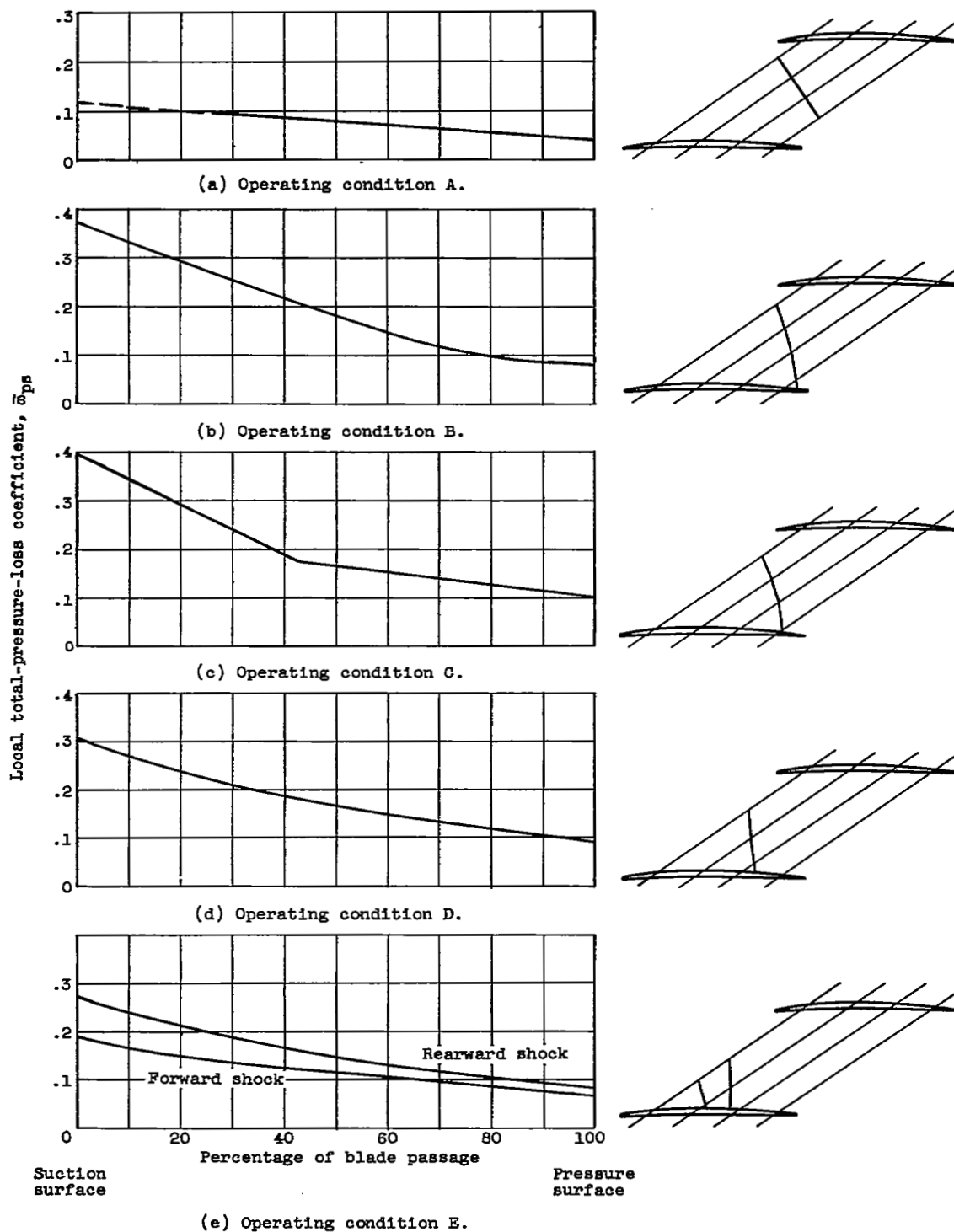


Figure 13. - Variation of estimated passage shock loss with percentage of blade passage from suction surface.

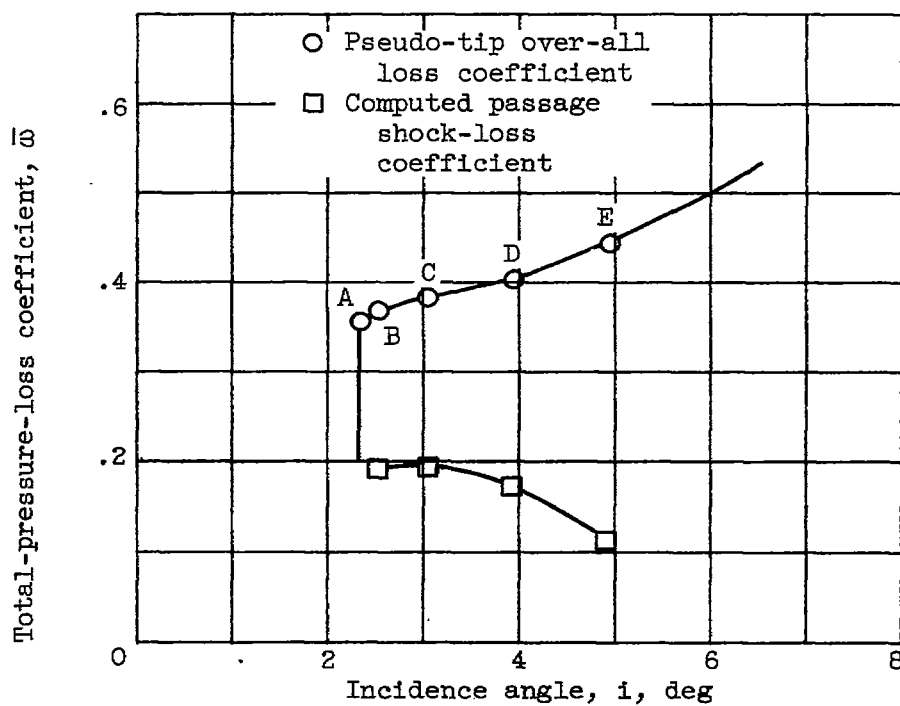


Figure 14. - Comparison of computed passage shock-loss coefficient with measured over-all loss coefficients at design speed.

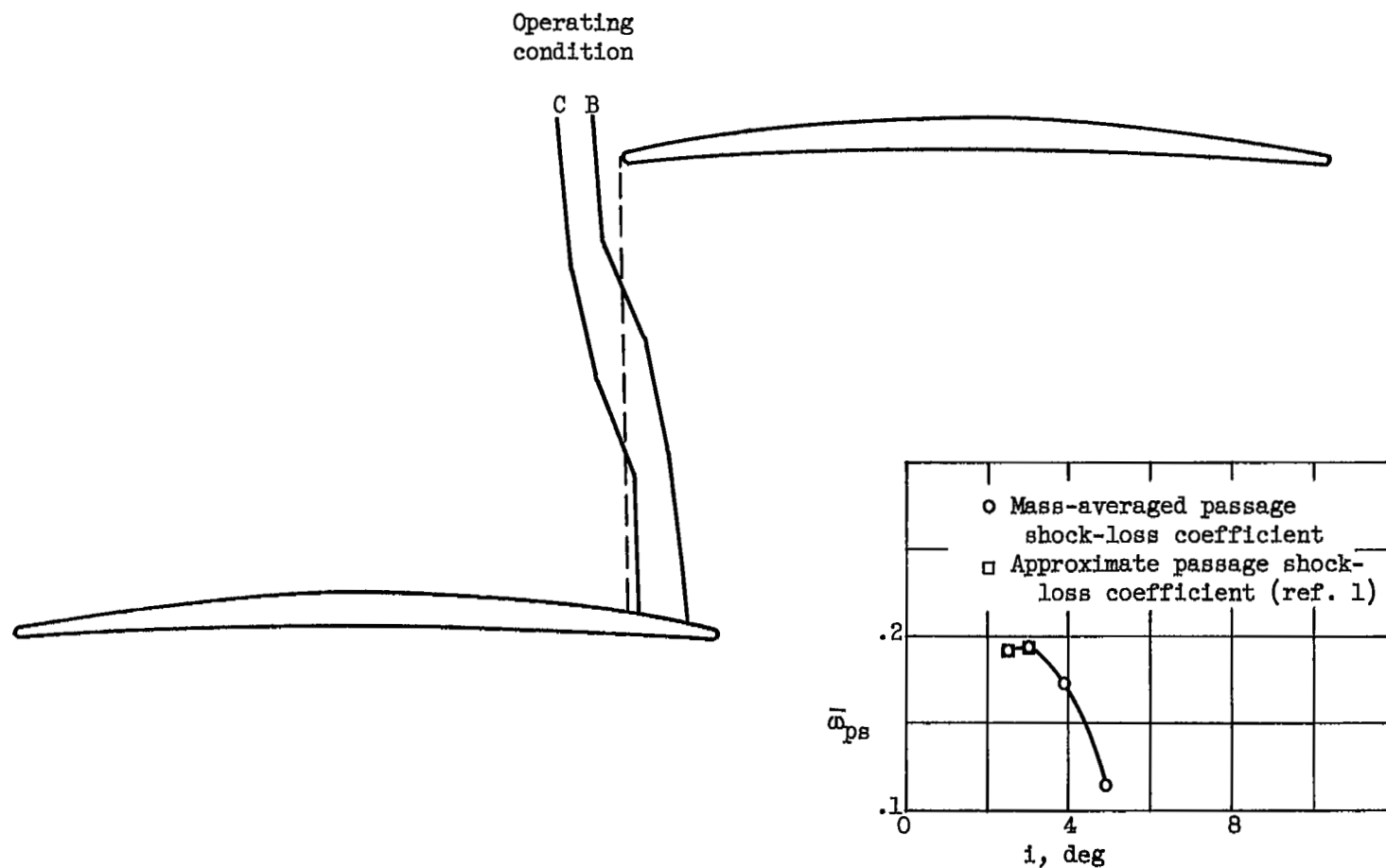


Figure 15. - Shock configurations and loss coefficients obtained with crystal probes compared with those obtained by simplified method of reference 1.

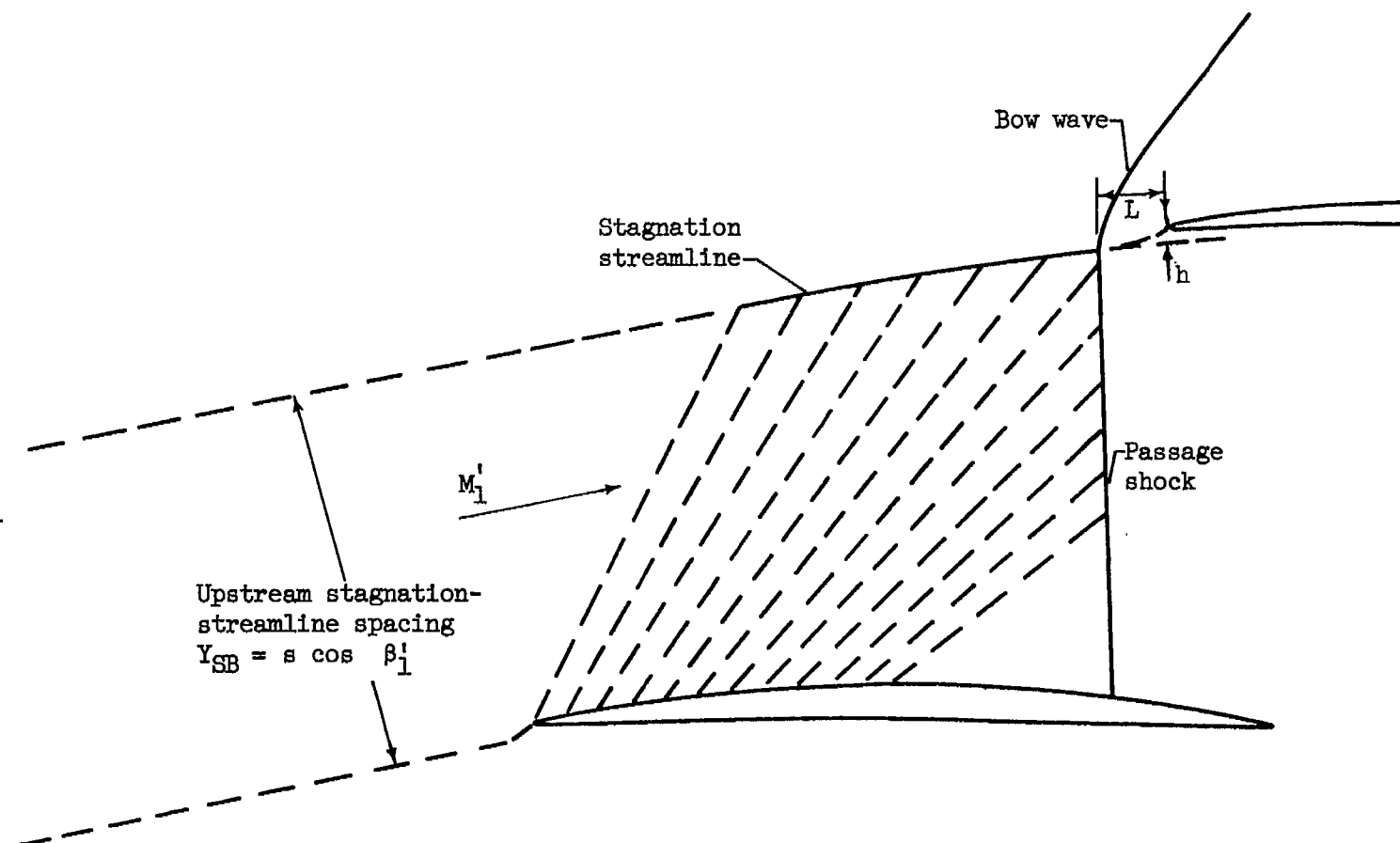
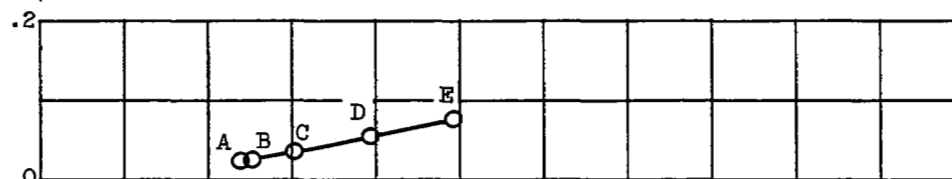


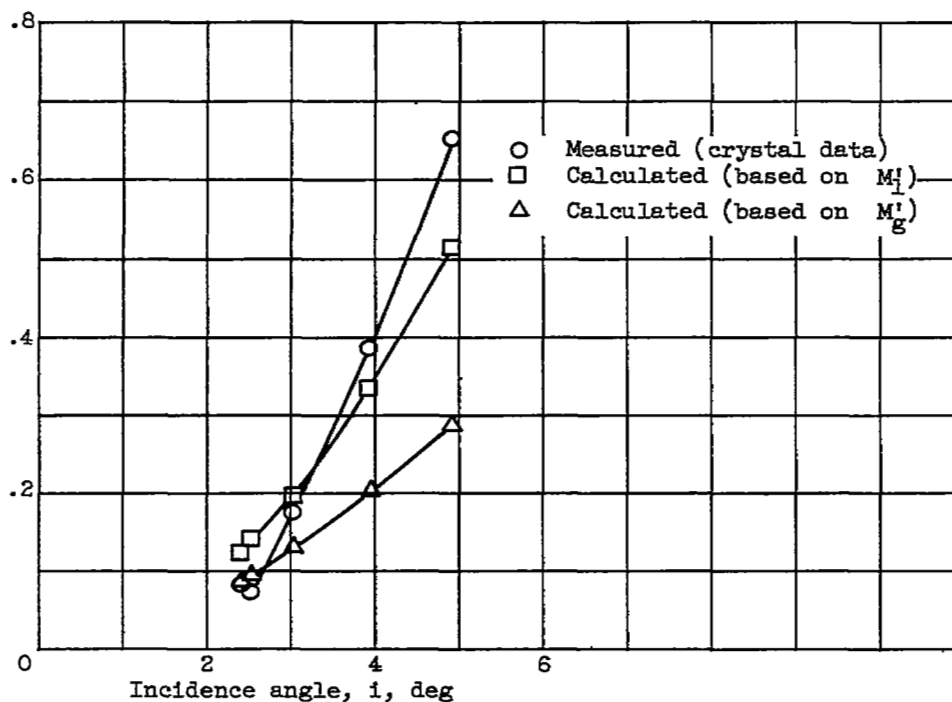
Figure 16. - Flow configuration assumed in inlet region to establish stagnation streamline through expansion region.

Dimensionless
height of blade
above stagnation
streamline,
 $\tau = h/Y_{SB}$



(a) Variation of h/Y_{SB} .

Dimensionless distance of bow wave
ahead of blade leading edge,
 L/Y_{SB}



(b) Variation of L/Y_{SB} .

Figure 17. - Comparison of measured and calculated dimensionless height of blade above stagnation streamline and distance of bow wave ahead of blade leading edge for range of incidence angles.

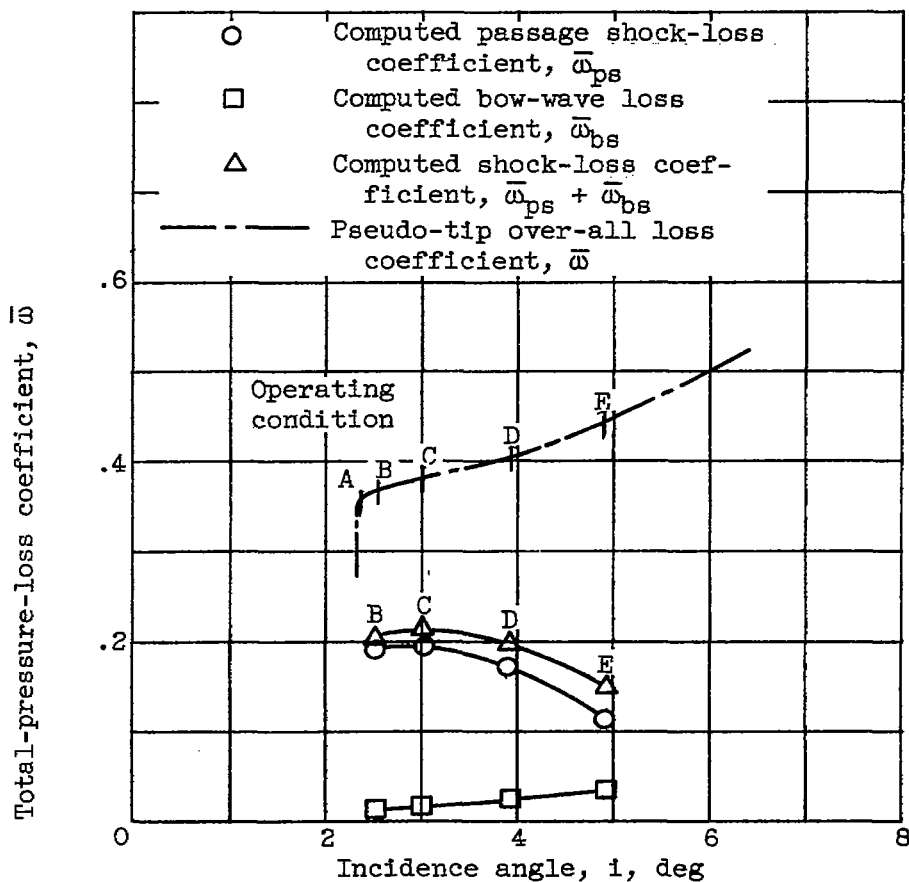


Figure 18. - Measured and computed total-pressure-loss coefficients for tip region at design speed.

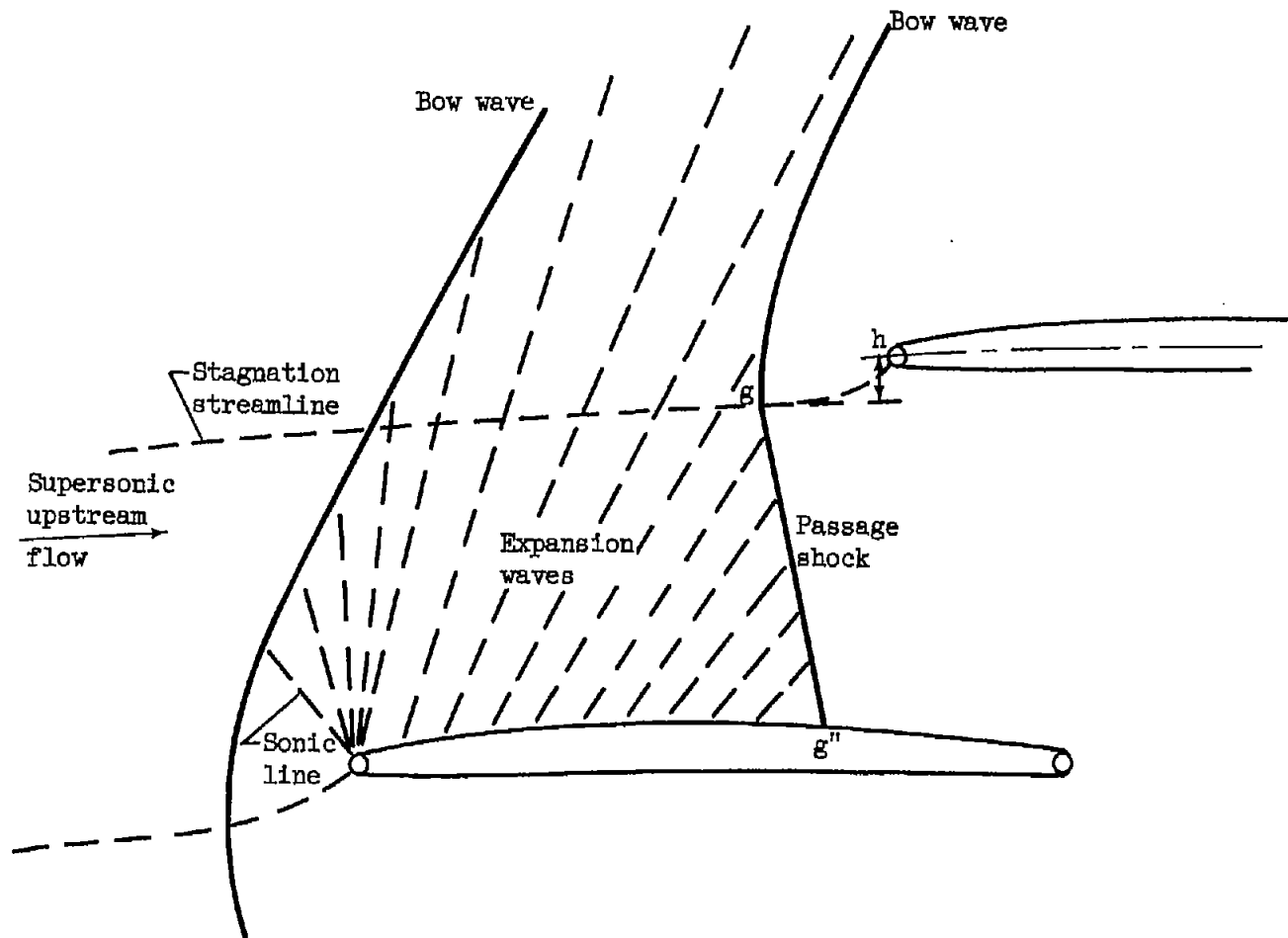
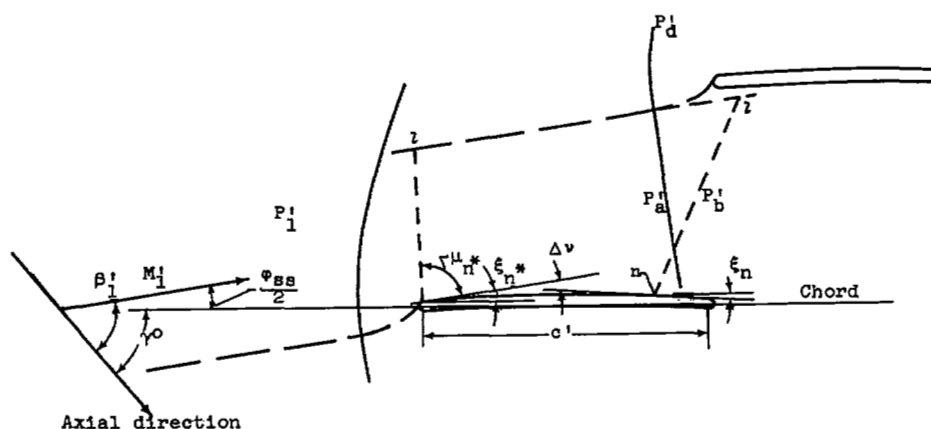
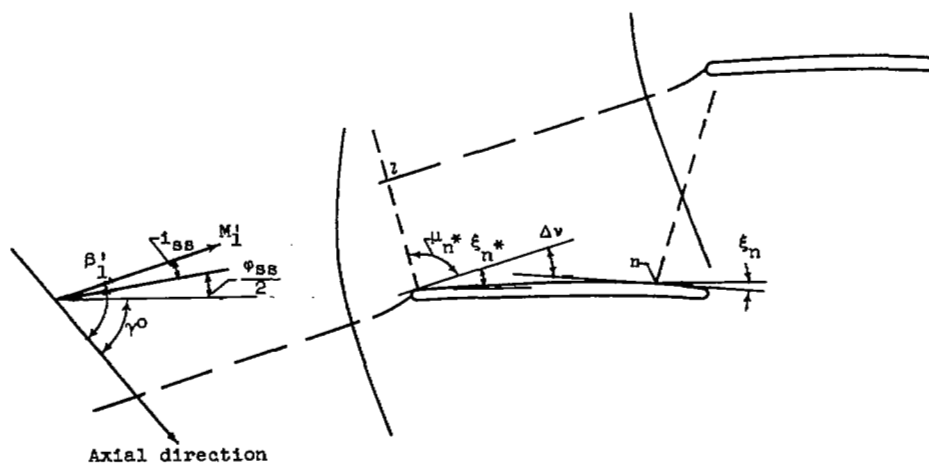


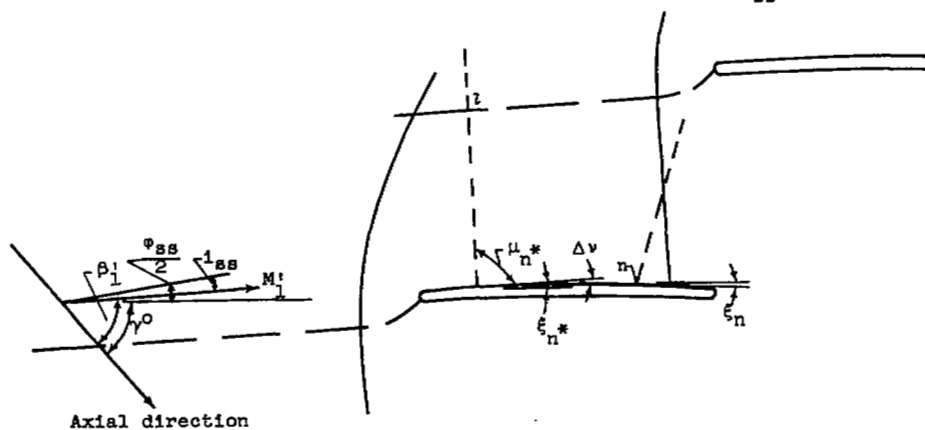
Figure 19. - Flow at inlet of cascade of airfoils operated with supersonic relative inlet Mach number.



(a) Inflow parallel to suction surface at blade leading edge; $i_{ss} = 0$.



(b) Inflow angle greater than angle of suction surface; $i_{ss} > 0$.



(c) Inflow angle less than angle of suction surface; $i_{ss} < 0$.

Figure 20. - Flow model illustrating geometry necessary to obtain flow conditions in supersonic region of cascade of blades at several inflow angles.

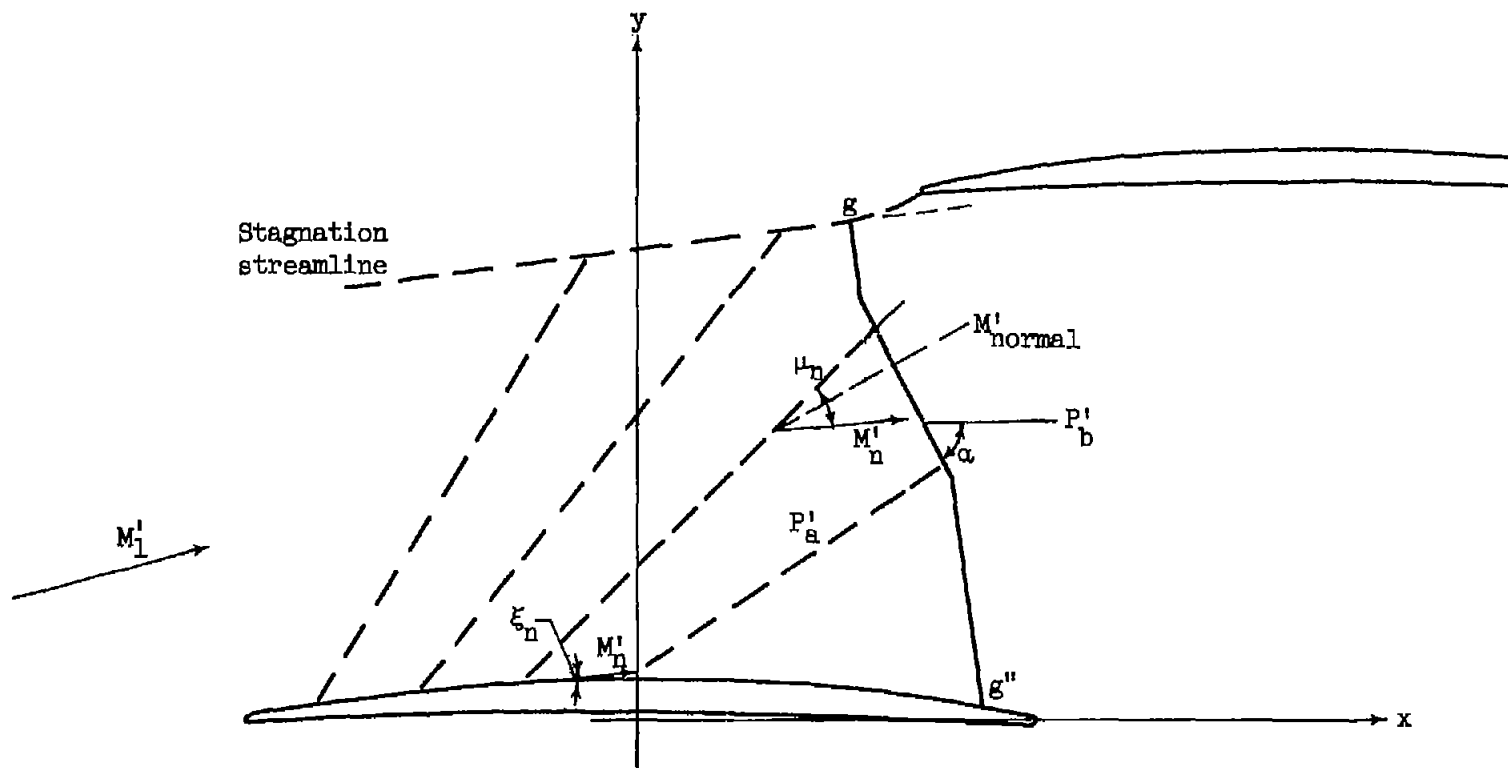


Figure 21. - Flow model showing geometry necessary for determining total-pressure ratio across passage shock of given location.

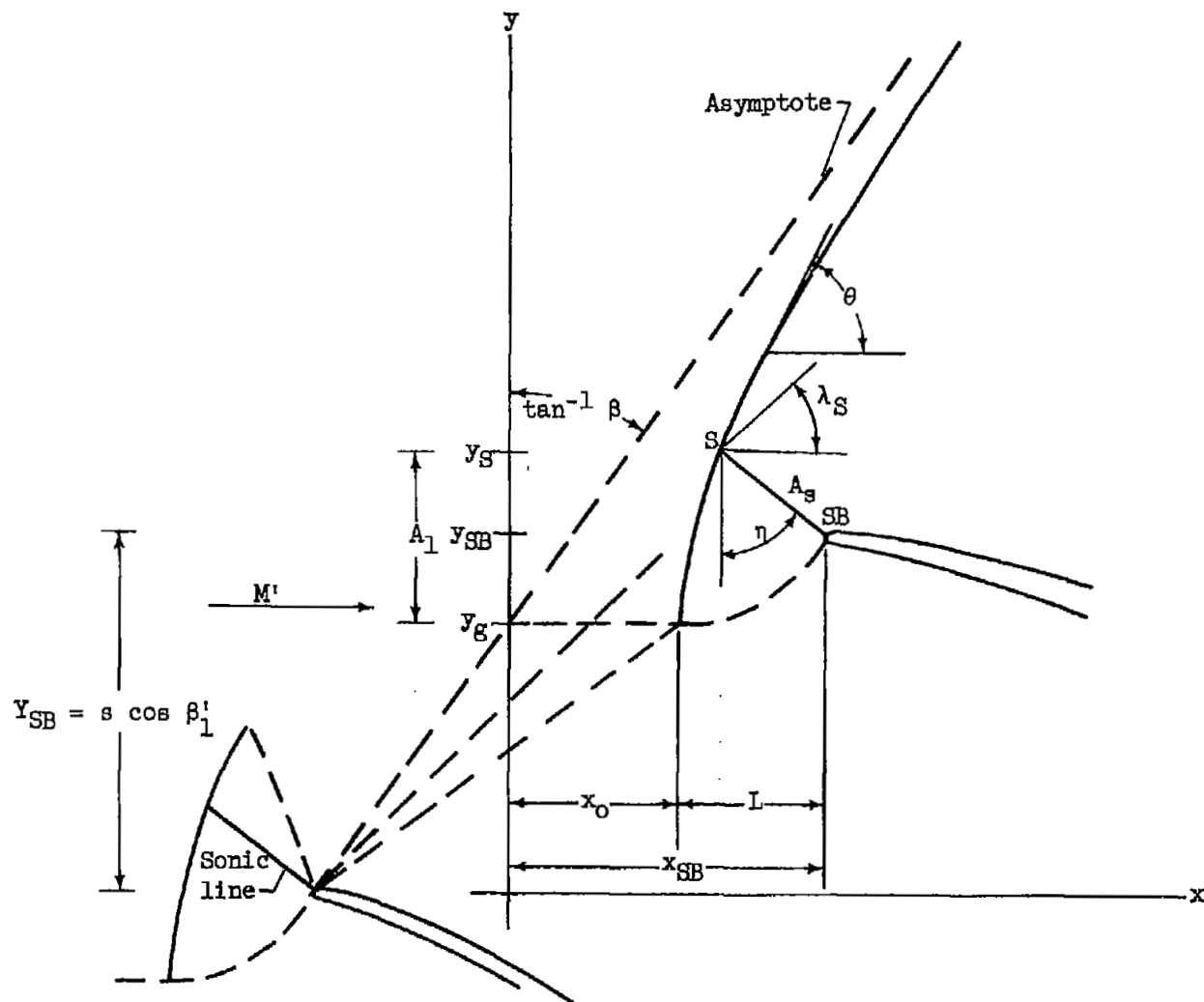


Figure 22. - Geometry necessary to establish bow-wave location for cascade of blades.

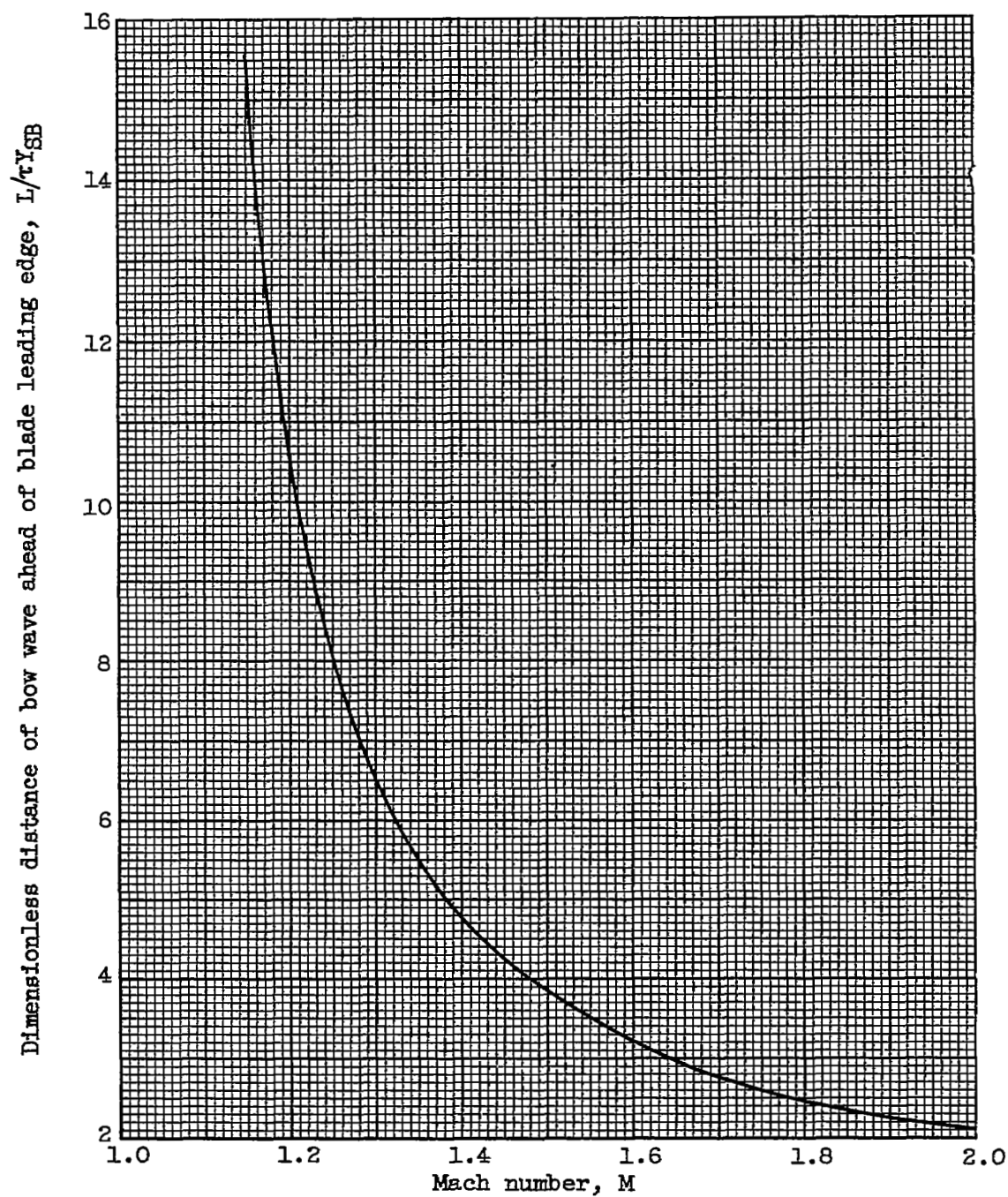


Figure 23. - Location of bow wave ahead of blade leading edge as a function of Mach number. (Fig. 7 of ref. 4.)

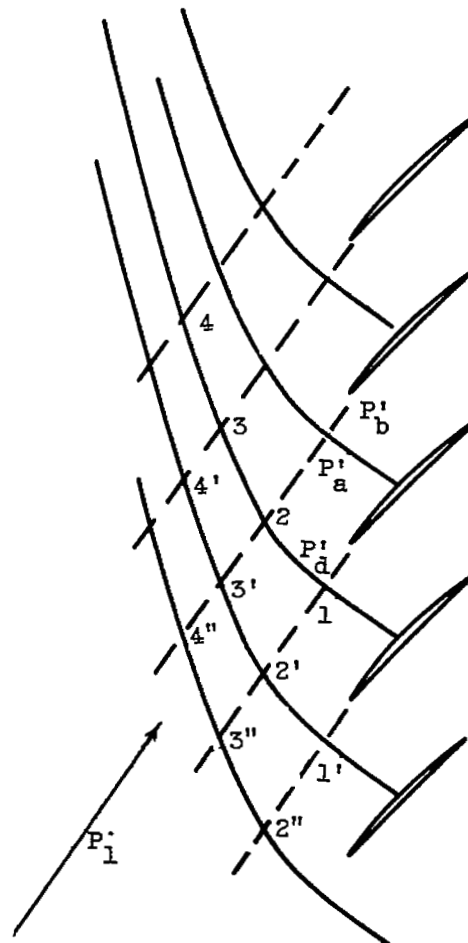


Figure 24. - Flow model showing bow waves caused by supersonic flow through a blade row.

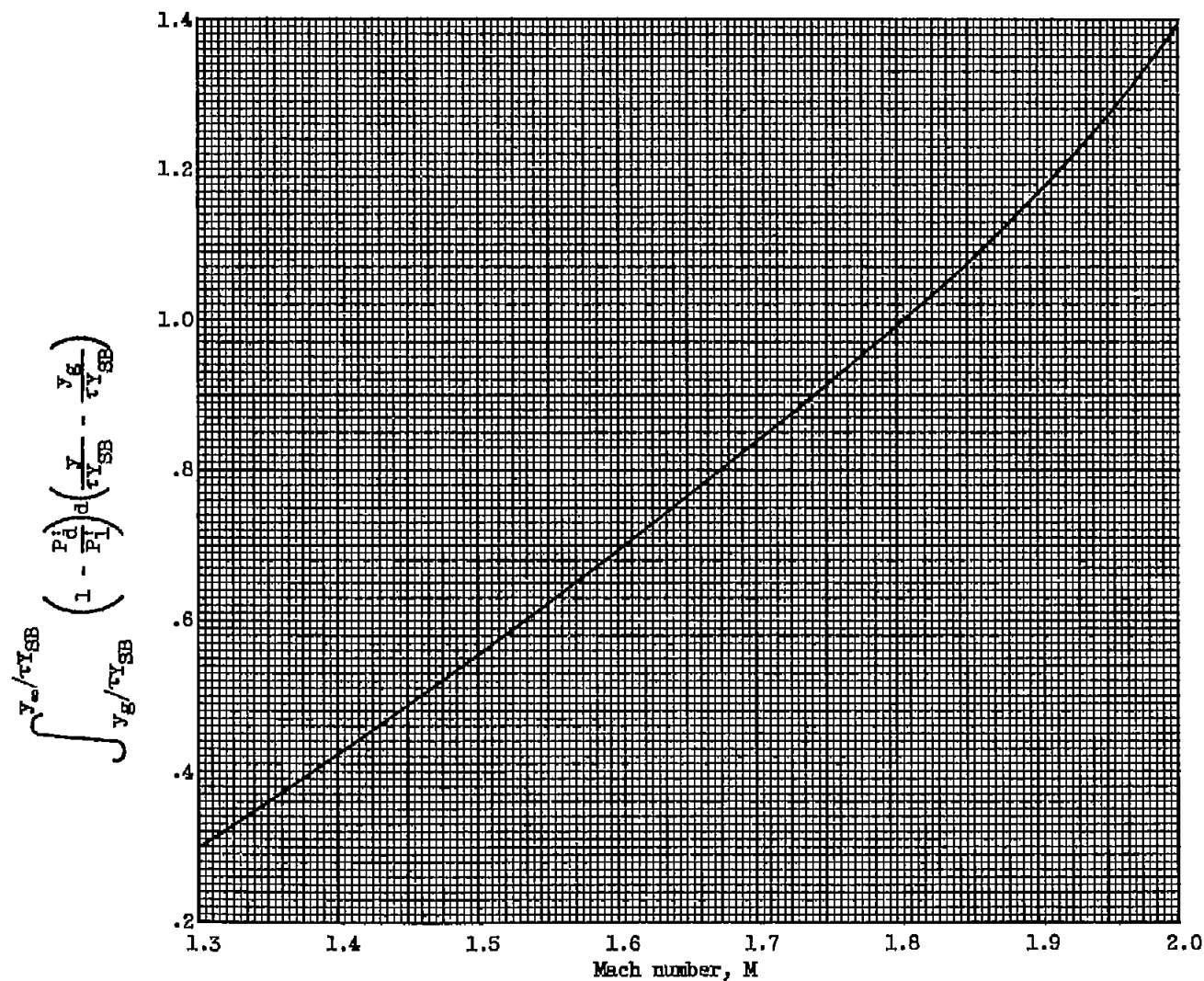


Figure 25. - Value of the integral necessary for evaluating bow-wave total-pressure loss. (Fig. 4 of ref. 6.)

NASA Technical Library



3 1176 01435 8981